Monthly Notices of the ROYAL ASTRONOMICAL SOCIETY

MNRAS **524,** 1291–1315 (2023) https://doi.org/10.1093/mnras/stad1900
Advance Access publication 2023 June 22

The MPIfR–MeerKAT Galactic Plane Survey – I. System set-up and early results

P. V. Padmanabh [1,2,3★] E. D. Barr,[1] S. S. Sridhar,[1,4] M. R. Rugel,[1,5,6] A. Damas-Segovia,[1] A. M. Jacob,[1,7] V. Balakrishnan [1] M. Berezina,[1,8] M. C. Bernadich,[1] A. Brunthaler,[1] D. J. Champion [1] P. C. C. Freire [1] S. Khan,[1] H.-R. Klöckner,[1] M. Kramer [1,9] Y. K. Ma [1,10] S. A. Mao [1] Y. P. Men,[1] K. M. Menten,[1] S. Sengupta,[1] V. Venkatraman Krishnan [1] O. Wucknitz,[1] F. Wyrowski,[1] M. C. Bezuidenhout [9] S. Buchner,[11] M. Burgay [12] W. Chen [1] C. J. Clark [2,3] L. Künkel,[13] L. Nieder [2,3] B. Stappers [9] L. S. Legodi [11] and M. M. Nyamai[11]

[1]*Max-Planck-Institut für Radioastronomie, Auf dem Hügel 69, D-53121 Bonn, Germany*
[2]*Max Planck Institute for Gravitational Physics (Albert Einstein Institute), D-30167 Hannover, Germany*
[3]*Leibniz Universität Hannover, D-30167 Hannover, Germany*
[4]*SKA Observatory, Jodrell Bank, Lower Withington, Macclesfield SK11 9FT, UK*
[5]*Center for Astrophysics | Harvard & Smithsonian, 60 Garden Street, Cambridge, MA 02138, USA*
[6]*National Radio Astronomy Observatory, PO Box O, 1003 Lopezville Road, Socorro, NM 87801, USA*
[7]*William H. Miller III Department of Physics and Astronomy, Johns Hopkins University, Baltimore, MD 21218, USA*
[8]*Landessternwarte, Universität Heidelberg, Königstuhl 12, D-69117 Heidelberg, Germany*
[9]*Jodrell Bank Centre for Astrophysics, Department of Physics and Astronomy, The University of Manchester, Manchester M13 9PL, UK*
[10]*Research School of Astronomy and Astrophysics, Australian National University, Canberra, ACT 2611, Australia*
[11]*South African Radio Astronomy Observatory, 2 Fir Street, Black River Park, Observatory 7925, South Africa*
[12]*INAF – Osservatorio Astronomico di Cagliari, Via della Scienza 5, I-09047 Selargius (CA), Italy*
[13]*Department of Physics and Astronomy, University of British Columbia, 6224 Agricultural Road, Vancouver, BC V6T 1Z1, Canada*

Accepted 2023 June 20. Received 2023 June 20; in original form 2023 March 15

ABSTRACT

Galactic plane radio surveys play a key role in improving our understanding of a wide range of astrophysical phenomena. Performing such a survey using the latest interferometric telescopes produces large data rates necessitating a shift towards fully or quasi-real-time data analysis with data being stored for only the time required to process them. We present here the overview and set-up for the 3000-h Max-Planck-Institut für Radioastronomie (MPIfR)–MeerKAT Galactic Plane Survey (MMGPS). The survey is unique by operating in a commensal mode, addressing key science objectives of the survey including the discovery of new pulsars and transients and studies of Galactic magnetism, the interstellar medium and star formation rates. We explain the strategy coupled with the necessary hardware and software infrastructure needed for data reduction in the imaging, spectral, and time domains. We have so far discovered 78 new pulsars including 17 confirmed binary systems of which two are potential double neutron star systems. We have also developed an imaging pipeline sensitive to the order of a few tens of micro-Jansky (μJy) with a spatial resolution of a few arcseconds. Further science operations with an in-house built S-band receiver operating between 1.7 and 3.5 GHz are about to commence. Early spectral line commissioning observations conducted at S-band, targeting transitions of the key molecular gas tracer CH at 3.3 GHz already illustrate the spectroscopic capabilities of this instrument. These results lay a strong foundation for future surveys with telescopes like the Square Kilometre Array (SKA).

Key words: pulsars: general – ISM: molecules – galaxies: magnetic fields.

1 INTRODUCTION

Galactic science has benefited vastly from large-scale surveys that maintain a balance between coverage and depth. In particular, observing the Galactic plane in the radio spectrum, spanning cm to (sub-)mm and near-infrared wavelengths through spectroscopy, polarization, imaging, and time domain has allowed for a thorough exploration of a range of Galactic phenomena. On one hand, they have delved into the early stages of the stellar cycle by probing dust and gas in regions with ongoing star formation (e.g. Benjamin et al. 2003; Taylor et al. 2003; Jackson et al. 2006; Stil et al. 2006; Caswell et al. 2010; Beltrán et al. 2013; Rigby et al. 2016; Su et al. 2019; Brunthaler et al. 2021), in particular also in the Southern sky (e.g. McClure-Griffiths et al. 2005; Schuller et al. 2009, 2021; Dickey et al. 2013), allowing for statistical studies of the evolution

★ E-mail: prajwal.voraganti.padmanabh@aei.mpg.de

of high-mass star formation (e.g. Urquhart et al. 2022). On the other hand, radio continuum Galactic plane surveys at centimetre wavelengths identified various sources in the final stages of the stellar cycle including supernova remnants (SNRs; e.g. see Dubner & Giacani 2015; Anderson et al. 2017; Dokara et al. 2021, 2022, and references therein) and planetary nebulae (e.g. Parker et al. 2006; Sabin et al. 2014). Besides total intensity continuum imaging, full Stokes polarized observations of the Galactic plane have been ideal to study magnetism and non-thermal emission in individual objects, including SNRs and H II regions (e.g. Kothes et al. 2006; Dokara et al. 2022; Shanahan et al. 2022). Moreover, thousands of neutron stars (NSs), formed in those supernova events, have been detected as radio pulsars in time-domain surveys focusing on the plane (e.g. Manchester et al. 2001; Cordes et al. 2006; Keith et al. 2010; Barr et al. 2013; Ng et al. 2015). One of the most recent examples is the Galactic Plane Pulsar Snapshot (GPPS) survey (Han et al. 2021) being conducted with the Five-hundred-meter Aperture Spherical Telescope (FAST; Li & Pan 2016) that has already found more than 500 new radio pulsars.[1] Advances in time-domain technology have also expanded the observable parameter space, opening up the potential for the discovery of new source classes within and beyond the Galaxy. A prime example is the discovery of fast radio bursts (FRBs; Lorimer et al. 2007). Several of these have been found in Galactic plane surveys, including the first repeating FRB (Spitler et al. 2014, 2016).

Besides targeted localized regions and individual sources, Galactic plane surveys have also mapped large-scale structures in the Galaxy. A fitting example is the Southern Galactic Plane Survey (SGPS; Haverkorn et al. 2006) that has used polarization to obtain the scale of fluctuations in the magnetic fields of the interstellar medium (ISM) and assess the magnetic field structure in the inner parts of the Galactic plane. Besides this, the Canadian Galactic Plane Survey (CGPS; Taylor et al. 2003) has continued to make significant contributions to the understanding of the global Galactic magnetic field (e.g. Rae & Brown 2010; Van Eck et al. 2021) by increasing the number of polarized sources known. These results are also important for polarization studies of extragalactic sources (e.g. Mao et al. 2014).

A consequence of studying small-scale and large-scale entities in the Galaxy is the development of interdependence between different fields, thus encouraging cross-disciplinary science. For example, SNRs identified in surveys may be searched in the hope of discovering pulsating NSs in their cores (similar to the Crab Pulsar; see Malov 2021, and references therein). Another example is using the polarization properties of pulsars to measure Faraday rotation, allowing for probing of the Galactic magnetic field along the lines of sight to these sources (e.g. Han et al. 2018; Abbate et al. 2020).

This cross-disciplinary nature also carries over to the observational and technical aspects of surveys. For example, spectral line studies and continuum imaging both use visibilities as the input data for their analysis pipelines. These visibilities only differ in bandwidth and spectral resolution. Surveys that offer both kinds of visibilities provide more holistic perspectives of different Galactic sources. For example, the Multi-Array Galactic Plane Imaging Survey (MAGPIS; Becker et al. 1994), The H I/OH/Recombination line survey of the inner Milky Way (THOR; Beuther et al. 2016), the Coordinated Radio and Infrared Survey for High-Mass Star Formation (CORNISH; Hoare et al. 2012) at 5 GHz, and the GLOSTAR survey at 4–8 GHz (Medina et al. 2019; Brunthaler et al. 2021) have helped understanding the radio spectral energy distribution at higher frequencies. This is essential for source characterization and for detecting sources of faint thermal emission. However, GLOSTAR and THOR also provide information on the atomic, molecular, and ionized gas content of these regions with spectral line measurements of H I, OH, H_2CO, CH_3OH, and multiple radio recombination lines. With this combined information, these surveys enable better understanding of the evolution of young high-mass stars and their surroundings (e.g. Brunthaler et al. 2021; Ortiz-León et al. 2021).

Although cross-disciplinary science is the common norm, commensal surveys incorporating a large range of scientific objectives have largely remained elusive owing to the inherent technical challenges. Early attempts were made by the Galactic Arecibo L-band Focal Array (GALFA) Collaboration to combine H I and pulsar search science into one commensal survey with the Arecibo telescope, but these did not succeed (see section 4 in Li et al. 2018, and references therein). However, modern observatories incorporate multiple backend processing systems that are capable of producing a range of calibrated scientific data products with various formats and resolutions, simultaneously. Recently, the Commensal Radio Astronomy FAST Survey (CRAFTS; Li et al. 2018) has been able to demonstrate such a capability, using a drift-scan mode to conduct H I imaging, pulsar, and FRB searches using at least four different backends. This has set a precedent for telescopes (single dish and interferometers) to enable similar operational modes for the future.

The MeerKAT radio telescope located in the Karoo desert of South Africa is a suitable telescope for carrying out such a commensal survey. Consisting of 64 dishes (with a diameter of 13.5 m each) that are spaced out with a maximum baseline of 8 km, the MeerKAT interferometer is currently the most sensitive radio telescope in the Southern hemisphere with a total gain of 2.8 K Jy^{-1}. Since achieving first light in 2016, the MeerKAT telescope has demonstrated its capability as an advanced instrument for science via large survey projects (LSPs)[2] covering aspects of time, imaging, and spectral line science. The Transients and Pulsars with MeerKAT (TRAPUM) project (Stappers & Kramer 2018) aimed at discovering radio pulsars and transients at specific targeted sources have yielded 184 discoveries at the time of writing.[3] MeerKAT has recently played an important role in producing a high-resolution mosaic image of the Galactic Centre at 1.28 GHz (Heywood et al. 2022). This image has revealed promising new SNR candidates and non-thermal filament complexes, thus demonstrating the superb imaging capabilities of the telescope. A fundamental requirement, necessary for the achievement of the scientific goals, is the state-of-the-art MeerKAT instrumentation, which provides the capability for beamforming, fine channelization (up to 32 000 channels spanning the entire bandwidth of 856 MHz), and generation of visibilities for imaging (Jonas & MeerKAT Team 2018). Finally, the MeerKAT telescope is a precursor to the Square Kilometre Array (SKA). The SKA-mid is one of the telescope arrays under SKA that will consist of ∼200 dishes operating between 350 MHz and 14 GHz. The MeerKAT set-up will be absorbed into this array.

The Max-Planck-Institut für Radioastronomie (MPIfR)–MeerKAT Galactic Plane Survey (MMGPS; see also Kramer et al. 2018) is a 3000-h multipurpose commensal survey being conducted with the MeerKAT radio telescope (Camilo et al. 2018; Jonas & MeerKAT Team 2018), covering science cases including pulsars,

[1] http://zmtt.bao.ac.cn/GPPS/GPPSnewPSR.html

[2] A full list of all LSPs is available at https://www.sarao.ac.za/large-survey-projects/

[3] More details on the discoveries, including some in this paper, are available at http://trapum.org/discoveries/

fast transients, Galactic magnetic fields, and targeted regions for continuum imaging, polarization studies, and spectral line diagnostics. The design of such a survey is informative for future observatories like the SKA (Dewdney et al. 2009) where telescope time management is key for maximal science outcome. The synergy between the different science cases allows for a feedback mechanism where the results from the imaging domain can have repercussions for the time-domain analyses and vice versa. This commensality between different fields also helps adapting to better strategies in an iterative manner as the survey progresses.

This paper describes the survey set-up and early results for each science case of the MMGPS. Section 2 discusses the key scientific objectives of the survey, based on the survey area that is chosen. Section 3 discusses the details of how the Galactic plane is being covered with various subsurveys. In Section 4, we describe the instrumentation used for conducting the survey. Section 5 discusses the observational set-up used for carrying out commensal observations. In Section 6, we describe the processing infrastructure implemented for the pulsar searches and the pipeline implemented for imaging analysis. Section 7 discusses specific areas that have enabled constructive feedback between different science cases while conducting commensal observations. In Section 8, we describe the new pulsar discoveries and discuss some of their properties. Section 9 describes early commissioning results from the continuum imaging and spectral line study aspects of the survey. Section 10 summarizes the progress of the survey so far and discusses the scientific prospects that lie ahead. We state our conclusions in Section 11.

2 KEY SCIENTIFIC OBJECTIVES

Based on the survey set-up explained in the previous section are the key scientific drivers across the time, imaging, and spectral line domains of the MMGPS described in detail below.

2.1 Discovering and analysing new pulsars

The pulsar search component of the survey builds on the high success rate of previous Galactic plane surveys like the Parkes Multibeam Pulsar Survey (PMPS, with more than 800 discoveries; Manchester et al. 2001), the Pulsar survey with the Arecibo L-band Feed Array (PALFA; Cordes et al. 2006), the High Time Resolution Universe (HTRU) South low-latitude (Keith et al. 2010) and North low-latitude (Barr et al. 2013) surveys, and more recently the GPPS survey (Han et al. 2021). The primary pulsar science objective of the MMGPS is to find previously undetected compact relativistic binary pulsars along the Galactic plane. Such systems probe gravity in the strong-field regime, allowing for tests of general relativity and alternative theories of gravity (e.g. Kramer et al. 2006, 2021). Furthermore, they provide improved constraints on frame dragging effects (Wex & Kopeikin 1999) and relativistic spin–orbit coupling (see e.g. Venkatraman Krishnan et al. 2020, and references therein). The continued opportunity for the discovery of such systems is demonstrated by the recent discoveries of PSR J1757−1854 (Cameron et al. 2018) and PSR J1946+2052 (Stovall et al. 2018), the most accelerated binary pulsars to date.

Such double neutron star systems (DNSs) also provide insight into binary evolution and the different formation channels for isolated and binary NSs (Tauris et al. 2017). Apart from DNSs, the Galactic plane pulsar searches are further motivated by the possible discovery of a pulsar–black hole binary following the discovery of a NS–black hole coalescence (Abbott et al. 2021). Although such a system has so far eluded discovery, it offers a range of scientific possibilities including stringent tests of general relativity and a direct measurement of the black hole spin, thus testing the cosmic censorship conjecture and 'no hair' theorem (Wex & Kopeikin 1999; Kramer et al. 2004; Liu et al. 2014). Besides tests of gravity, the discovery of a sample of binary pulsar systems offers the potential for the precise determination of NS masses. Such masses contribute to an improved understanding of the formation of NS and supernova physics (Tauris et al. 2017); furthermore, the largest NS masses (Antoniadis et al. 2013; Fonseca et al. 2021) yield tight constraints on the equation of state of superdense matter (see Özel & Freire 2016, for a review).

Additionally, the MMGPS aims to increase the population of pulsars in the Galactic Centre region with the highest priority being the discovery of a pulsar orbiting the central supermassive black hole Sagittarius A* (Sgr A*). The small number of pulsars discovered in the Galactic Centre region so far (six known pulsars in a 70 pc radius around Sgr A*; Johnston et al. 2006; Deneva, Cordes & Lazio 2009; Eatough et al. 2013b) raises questions about the current estimates of NS birth rates around this region (Wharton et al. 2012). It could also indicate that propagation effects are a major hurdle in the detection of such systems. Recent searches conducted at high frequencies ranging from 4 to 154 GHz with three different telescopes, the Effelsberg 100-m telescope, IRAM 30-m telescope, and the Atacama Large Millimeter/submillimeter Array (ALMA), have yielded no new pulsars (Eatough et al. 2021; Liu et al. 2021; Torne et al. 2021). The unsuccessful searches have been attributed to interstellar propagation effects like dispersion and scattering coupled with the steep spectral indices of pulsars proving to be a major limitation. Despite a poor yield so far, the numerous scientific possibilities coupled with improved sensitivity from MeerKAT motivate the continuation of pulsar searches around the Galactic Centre. Additionally, the usage of receivers at S-band (1.7–3.5 GHz) allows for deep searches along the Galactic plane where the severe dispersion ($\tau_{\rm d} \propto \nu^{-2}$, where $\tau_{\rm d}$ is the dispersive delay and ν is the observing frequency) and scattering ($\tau_{\rm s} \propto \nu^{-4.4}$ assuming Kolmogorov turbulence, where $\tau_{\rm s}$ is the scattering time-scale) effects are significantly reduced.

A discovery of a pulsar in a tight orbit around Sgr A* would be an ideal probe for understanding the gravitational influence of a supermassive black hole and the environment surrounding Sgr A* (see Kramer et al. 2004; Bower et al. 2019, and references therein). Although the current set of pulsars near the Galactic Centre region (except the Galactic Centre magnetar: PSR J1745−2900) is relatively distant from Sgr A* ($> 0.1^{\rm o}$ or 15 pc), these pulsars have found a wide range of use cases. For example, previous discoveries have allowed for a better understanding of the magneto-ionic environment around the Galactic Centre region (Desvignes et al. 2018). Additionally, studying their spin-down rates has helped to constrain the gravitational potential at the centre of the Galaxy (e.g. Kramer et al. 2006; Perera et al. 2019).

The scope for additional pulsar science cases is summarized below.

(i) Discovery of pulsars that resolve open questions regarding binary evolution. A prime example is the existence of a variety of eccentric millisecond pulsars (MSPs) in the Galactic plane (see table 1 in Serylak et al. 2022) that has led to multiple theories explaining eccentric MSP formation (e.g. Freire et al. 2011; Antoniadis 2014; Freire & Tauris 2014; Jiang et al. 2015) with no clear evidence for a single theory that explains all such currently known systems (Serylak et al. 2022).

(ii) Discovery of pulsars with atypical emission properties including intermittency (e.g. Lyne et al. 2017), drifting subpulses (see e.g. Szary et al. 2020, and references therein), nulling, and mode switching (see e.g. Ng et al. 2020, and references therein) provides

observational grounds on which the pulsar emission mechanism can be studied and constrained (see Philippov & Kramer 2022, for a review).

(iii) Improving population models through the discovery of a large number of new canonical pulsars and MSPs (e.g. Faucher-Giguère & Kaspi 2006; Lorimer 2013; Lorimer et al. 2015). The added advantage here is the use of S-band that can help mitigate biases introduced in population models due to the majority of pulsar surveys being conducted at lower frequencies (1.4 GHz and below).

(iv) Enhancing detection capabilities of pulsar timing arrays (PTAs) of the nanohertz gravitational wave background through discoveries of MSPs with stable timing properties (see Dahal 2020, for a review). The recent detection of a correlated red-noise term between PTA pulsars has proven that any improvements in sensitivity in the future can increase the detection probability (e.g. Antoniadis et al. 2022). Furthermore, long-term timing of potential nearby fast spinning pulsar discoveries can constrain the parameter space for targeted continuous gravitational wave searches (e.g. Ashok et al. 2021).

2.2 Magnetism science

The primary motivation behind the imaging and polarization aspects of the MMGPS is to increase the number of known Galactic and extragalactic polarized sources (both compact and diffuse) and in turn improve the understanding of Galactic magnetic fields.

The discovery of extreme rotation measure (RM) values along the Sagittarius Arm in THOR survey at 1–2 GHz (Shanahan et al. 2019) suggests that RM values upwards of a few thousand rad m^{-2} can be found towards background extragalactic sources along tangent points of spiral arms. This is likely due to compression of the warm ionized medium by the spiral density wave (Gaensler et al. 2008; Langer et al. 2017; Reissl et al. 2020). Fully characterizing the extent and the magnitude of extreme RM regions in both Galactic longitude and latitude helps to gain a full understanding of the origin of these spikes in the integral of the product of thermal electrons and magnetic fields. Any new discoveries will demonstrate that extreme Faraday rotation is indeed a global feature in the Milky Way and will enable further understanding of its origin and its implications on the overall properties of Milky Way magnetic field.

A recent RM study along the Galactic plane ($|b| < 5^\circ$) towards part of the first Galactic quadrant (specifically, $20^\circ < \ell < 52^\circ$) has found that the RM of background extragalactic sources are asymmetric about the Galactic mid-plane in the longitude range of about 40°–52° (Ma et al. 2020). The favoured explanation is that the Galactic disc magnetic field in the Sagittarius spiral arm has an odd-parity, with the plane-parallel component of the magnetic field switching in direction across the mid-plane. This is in contrast to the expected magnetic field structure of the Galactic disc from the α–Ω dynamo (e.g. Ruzmaikin, Sokolov & Shukurov 1988; Beck et al. 1996). Similar future studies of the RM structures towards the other spiral arms, especially those in the Southern sky that have historically been sampled with a significantly lower RM source density (see below), will be crucial to our knowledge of the magnetic structures of the Galactic disc and our understanding in the amplification and ordering processes of the magnetic fields in galaxies. The case of the Carina arm (tangent point at $\ell \approx 283^\circ$; Vallée 2022) is particularly interesting, as it is the southern extension of the Sagittarius spiral arm.

The high spatial resolution and sensitivity of the MMGPS (leading to an expected density of ∼25 RM source deg^{-2}) will enable the refinement of the RM grid technique (see e.g. Rudnick 2019). Existing Galactic magnetic field models in Galactic quadrant 4 were previously developed based on a sparse grid of Faraday rotation measurements of extragalactic radio sources with a density of ∼0.2 deg^{-2} from the SGPS (Brown et al. 2007). The expected increase in the RM grid density of approximately two orders of magnitude will robustly reveal the magnetic field symmetry across the Galactic mid-plane (see above), as well as the direction and the strength of magnetic fields along Carina, Scutum-Crux, Norma arms, and in the molecular ring. This allows one to robustly establish the Galactic magnetic field structure, knowledge of which is critical for our understanding of the origin and evolution of magnetic fields in galaxies (Johnston-Hollitt et al. 2015; Heald et al. 2020). Meanwhile, the small-scale magnetized gas properties can be probed via both the structure function analysis of the RM grid (down to few 10 pc at a distance of few kpc; e.g. Xu & Han 2019) and the broad-band linear polarization modelling of the detected sources (on sub-pc scales; e.g. Anderson et al. 2015; Livingston et al. 2021).

An RM grid produced in the Galactic Centre region will be sensitive to extreme values of RMs (up to 2×10^6 rad m^{-2} in magnitude), as such values are expected towards the Galactic Centre and have indeed been seen toward the Galactic Centre magnetar (-7×10^4 rad m^{-2}; Eatough et al. 2013b). Utilizing the S-band for this purpose also implies that the λ^2-dependent depolarization is minimal (λ denotes the observing wavelength). Additionally, prominent non-thermal filaments in the field of view can be better studied with Faraday tomography (e.g. Paré et al. 2021). The previous best published (narrow-band) RM grid within 0.°5 (or 70 pc) of the Galactic Centre only comprised a handful of RMs (Roy, Pramesh Rao & Subrahmanyan 2008). One expects an order of magnitude increase in the density of the RM grid, combined with RM and dispersion measure (DM) of pulsars for both existing (Schnitzeler et al. 2016) and those discovered from the MMGPS. This will yield important insight into the complex magnetic structures in the immediate vicinity of the Galactic Centre and its connection to the global Galactic magnetic field.

Finally, the catalogue of polarized sources obtained (estimated to be >5000) will offer the best λ^2 coverage across L-band (0.8–1.7 GHz) and S-band (1.7–3.5 GHz) at the highest spatial resolution in the GHz regime in the pre-SKA era. This will provide a platform for statistical characterization of intrinsic polarization properties of extragalactic radio sources and will further enable the extraction of physical properties of the magneto-ionic medium in and around these sources (Schnitzeler et al. 2019). Such a large sample can help to understand whether and how the intrinsic polarization fraction, depolarization, and Faraday complexity depend on various source properties, such as their radio luminosity, total intensity properties, radio source type, morphology, environment, redshift, and other multiwavelength characteristics. Moreover, the dual frequency band coverage will provide spectral index information on all sources and will serve as a source list for other science cases (see next section).

2.3 Galactic interstellar medium and star formation

With several Galactic plane surveys from near- over far-infrared to (sub)millimetre wavelengths covering dust and molecular gas at subarcminute resolution, complementary high-resolution surveys at longer radio wavelengths are essential to obtain a comprehensive view of the star formation process at small angular scales.

One of the main scientific goals from the perspective of the Galactic interstellar medium (ISM) is the identification of tracers for different stages of the star formation cycle. In the radio range, this ranges from studies of neutral and ionized gas to the

Table 1. Spectroscopic properties of the CH ground state hyperfine structure (HFS) transitions. The columns are (from left to right): the transition as described by the hyperfine quantum number (F), the frequency of the transition, the Einstein A coefficient, and the relative line intensities at local thermodynamic equilibrium (LTE). The frequencies were measured by Truppe et al. (2014) with uncertainties of 3 Hz.

Transition F'–F''	Frequency (MHz)	A_E $\times 10^{-10}$ (s^{-1})	Relative intensity
0^-–1^+	3263.793447	2.876	1.0
1^-–1^+	3335.479356	2.045	2.0
1^-–0^+	3349.192556	1.036	1.0

compact, ultracompact, and hypercompact H II regions (UCH II/HCH II regions) excited by high-mass young stellar objects, which probe different stages of early stellar evolution, to SNRs and planetary nebulae (PNe) giving insights in to the final stages of star formation. The spectral index and polarization information provided from continuum imaging (as described in the previous section) allows one to distinguish between non-thermal and thermal emission enabling the detection of optically thick emission from UCH II and HCH II regions, and enabling the search for non-thermal jets from massive young stellar objects (e.g. Moscadelli et al. 2019). Additionally, the surface brightness sensitivity of MeerKAT will map the diffuse emission around UCH II and HCH II regions, which is critical for studying the environment of these early phases of massive star formation (e.g. Kurtz et al. 1999).

The MMGPS can build on previous/existing surveys probing similar regions in the Galaxy. For example, the 4–8 GHz Galactic plane survey GLOSTAR (Brunthaler et al. 2021) aimed to characterize star formation in the Milky Way conducted by the MPIfR using the Karl G. Jansky Very Large Array (JVLA) and the Effelsberg 100-m telescope is an excellent counterpart to MMGPS for the Northern skies. The ATLASGAL sub-mm dust continuum survey (also conducted by the MPIfR) with the APEX 12-m submillimetre telescope at 870 μm ($|l| < 60°$; $|b| < 1°.5$; Schuller et al. 2009) and its molecular line follow-up programs is another such example. The properties of multiple UCH II and HCH II regions that will be detected are strongly related to the physical conditions of their parental clumps, which have been determined in the ATLASGAL survey (e.g. Urquhart et al. 2018, 2022), and will provide information on the embedded population of H II regions in dense clumps. In combination with mid-infrared images (e.g. GLIMPSE; Benjamin et al. 2003), these H II regions will be classified and compared to their parent clumps (e.g. Urquhart et al. 2013).

The high-frequency end of S-band covers the hyperfine structure (HFS) split lines of the CH radical between the Λ-doublet levels of its rotational ground state at 3.3 GHz (frequencies are summarized in Table 1). In addition to being an important intermediate in interstellar carbon chemistry, observations of CH at ultraviolet (UV)/optical and later far-infrared observations of CH have established its use as a surrogate for H_2 in diffuse and translucent clouds particularly in CO-dark molecular gas (e.g. Federman 1982; Sheffer et al. 2008; Weselak 2019). The radio lines of CH first detected by Rydbeck, Elldér & Irvine (1973) were observed in wide-spread (generally weak) emission toward a variety of different environments ranging from dark clouds to H II regions (Zuckerman & Turner 1975; Rydbeck et al. 1976; Lang & Wilson 1978; Genzel et al. 1979; Whiteoak, Gardner & Hoglund 1980; Mattila 1986; Sandell, Magnani & Lada 1988; Magnani, Sandell & Lada 1992; Magnani & Onello 1993). Despite being ubiquitously observed, the relative intensities of the ground state radio HFS lines of CH were found to be inconsistent with assumptions of local thermodynamic equilibrium (LTE) and always observed in emission, even against continuum sources (see Table 1). This suggested that the populations of the CH ground state Λ-doublet HFS levels must be inverted. While this can be qualitatively understood via a general pumping cycle that involves collisional excitation processes, the relative intensities of the lines and in particular the dominance of the lowest frequency satellite line has not been well understood, thereby limiting the use of the CH radio emission as a tracer of the molecular ISM.

Recently, Jacob et al. (2022) investigated the excitation responsible for causing anomalous excitation and level inversion in the CH ground state aided by the latest HFS-resolved collisional rate coefficients (Dagdigian 2018; Marinakis et al. 2019). Additional constraints were placed on the models using reliable column densities provided by far-infrared transitions of CH that shares a common lower energy level with the radio lines, observed using the upGREAT (Risacher et al. 2016) receiver onboard the Stratospheric Observatory for Infrared Astronomy (SOFIA; Young et al. 2012) telescope. The modelled results establish the use of CH as a powerful radio-wavelength probe of diffuse and translucent clouds in the ISM. The combined modelling of the radio and far-infrared observations can further constrain the physical properties of the gas traced by CH and manifest CH as a probe of the diffuse ISM over Galactic scales.

3 SURVEY LAYOUT

Based on the key science objectives presented in the previous section and an allocated time budget of 3000 h, we have divided the survey into several subsurveys. In this section, we give a brief introduction to each of these subsurveys. The footprints of some subsurveys are shown in Fig. 1and the specifications of each subsurvey are summarized in Table 2. The different subsurveys are described below.

(i) *Shallow L-band Galactic Plane Survey (MMGPS-L).* This survey consists of 10-min integrations covering a wide area (approximately 936 deg^2) of the Galactic plane. This 800-h survey uses the superior gain of MeerKAT to discover pulsars that are either too faint to be have been detected by previous searches or only emit intermittently. Besides this, the short integration time ensures reasonable sensitivity to compact binary pulsars with an orbital period of ∼2 h (e.g. Ransom, Cordes & Eikenberry 2003). From the continuum observations perspective, the survey at L-band (856–1712 MHz) provides the widest frequency coverage and superior angular resolution (down to 7 arcsec), sensitivity and surface brightness sensitivity compared to existing/planned surveys at L-band in the Southern sky (e.g. the SGPS, McClure-Griffiths et al. 2001; the POSSUM survey, Gaensler et al. 2010). The region covered in L-band also includes spiral arm regions with a particular focus on the Carina arm (the southern extension of the Sagittarius Arm) at longitude 282°–287°. This will help better characterize the extent and the magnitude of extreme RM regions. The frequency resolution of 0.417 MHz at L-band allows for the detection of polarized sources with Faraday rotation magnitudes up to at least 3.3×10^4 rad m^{-2} at L-band. Henceforth, we refer to this subsurvey as the MMGPS-L.

(ii) *Deep S-band Galactic Plane Survey (MMGPS-S).* This forms the largest portion of the MMGPS survey requiring 1380 h of observation. The survey coverage is 285 deg^2 and focused on maximizing the Galactic longitude coverage at the expense of latitude coverage (see Table 2). A centre frequency of 2406.25 MHz is used with an integration length fixed at 20 min. The primary driver

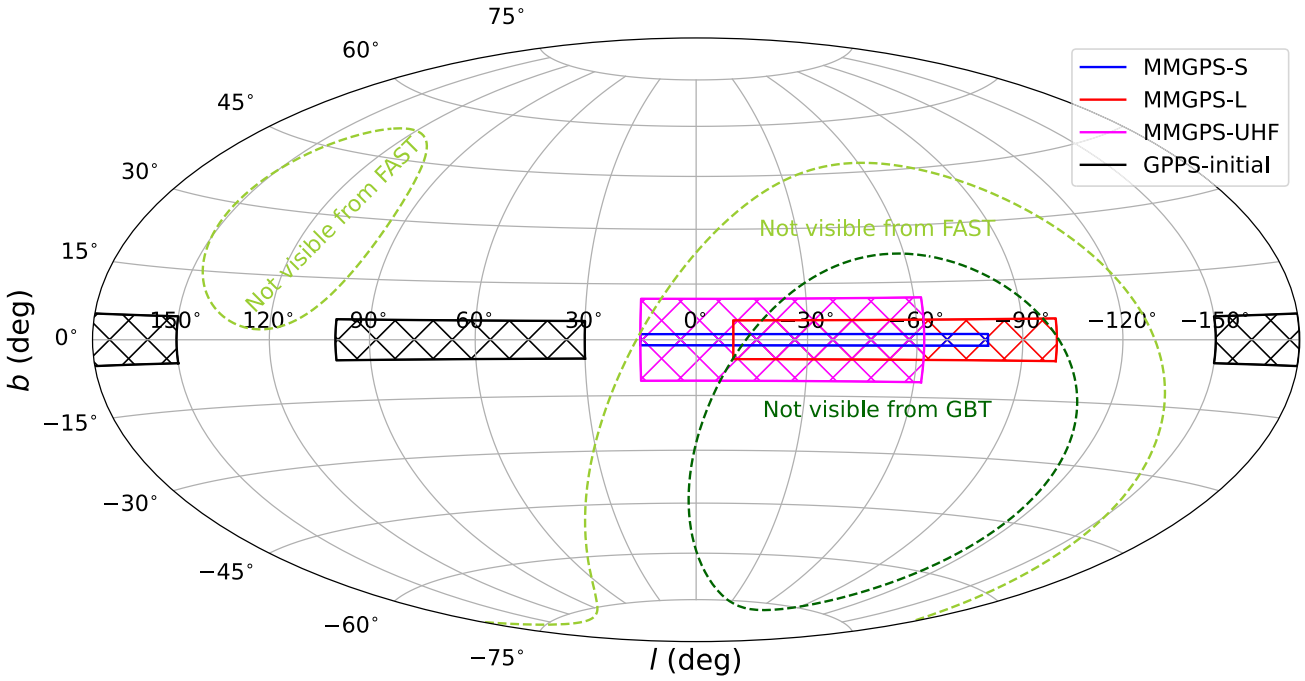

Figure 1. The survey region layout for the latest and most sensitive Galactic plane surveys. The red region indicates the L-band (0.85–1.7 GHz) portion of MMGPS, the magenta region indicates the UHF survey, and the blue region shows the deep S-band portion of the survey. It should be noted that certain regions have dual and triple frequency coverage (see Table 2). The coverage of the Galactic Plane Pulsar Snapshot survey with FAST (GPPS; Han et al. 2021) is shown for reference. The corresponding regions that are not visible from the Green Bank Telescope and FAST are also overlaid. The regions are calculated based on the declination limits imposed due to the respective observatory latitudes. MMGPS-Sgr A* and MMGPS-CH/H I/OH spectral line surveys are targeted at a fixed number of select sources and hence not included in this plot.

Table 2. The observation parameters of the four MMGPS subsurvey regions. The parameter $t_{\rm dwell}$ corresponds to the planned integration time for each subsurvey based on the time constraint and survey coverage limitations (see text). $N_{\rm chan}$ corresponds to the channel bandwidth in MHz, $t_{\rm samp}$ is the sampling time, and $\nu_{\rm centre}$ is the observation centre frequency.

Survey	Duration (h)	Latitude range (°)	Longitude range (°)	$t_{\rm dwell}$ (s)	Channel bandwidth (MHz)	$t_{\rm samp}$ (μs)	$\nu_{\rm centre}$ (MHz)
MMGPS-L	800	$\lvert b\rvert < 5.2$	$-100 < l < -10$	637	0.417	153	1284
MMGPS-S	1380	$\lvert b\rvert < 1.5$	$-80 < l < 15$	1274	0.854	153	2406.25
MMGPS-Sgr A*	200	$b = -0.05$	$l = -0.04$	1274	0.854	76	3062.5
MMGPS-UHF	400	$\lvert b\rvert < 11$	$-62 < l < 15$	505	0.132	120	816
MMGPS-CH/H I/OH	55	–	–	600/2400	0.003[a]	–	L- and S-band (see text)

[a]Valid currently for L-band only.

of this subsurvey is discovering compact binary pulsars along the Galactic plane that were previously missed due to limitations from ISM propagation effects. Thus, the average DM values of pulsar discoveries from this survey are expected to be higher than those made with MMGPS-L. While the survey at S-band will provide a similar/better RM grid density as MMGPS-L, its higher frequency coverage will overcome wavelength-dependent depolarization effects, allowing one to probe highly turbulent sightlines through the Galactic plane that are inaccessible to MMGPS-L or future SKA L-band surveys. The frequency resolution at S-band will allow detection of polarized sources with Faraday rotation magnitudes up to at least 3.3×10^5 rad m^{-2}. We refer to this survey as MMGPS-S hereafter.

(iii) *Ultra-Deep S-band Galactic Centre Survey (MMGPS-Sgr A*).* The remaining 200 h of the MMGPS are used for observations centred on Sgr A*. This survey is conducted at the high-frequency end of S-band (i.e. 3062.5 MHz) in order to minimize the impact of deleterious ISM propagation effects. At this frequency the S-band primary beam width is $\sim 0.^{\circ}5$ and thus will cover a $\sim$0.2 deg^2 field. Assuming that the Galactic Centre is $\sim$8.1 kpc away (Gravity Collaboration et al. 2019), the primary beam spans 70.65 pc. The corresponding tied-array beam at the high end of S-band is $\sim$3 arcsec in size (assuming boresight) that implies that the best achievable localization is 0.5 pc around Sgr A*. To further exploit the richness of these data, multiple observations will be combined post-facts to perform extremely deep searches for pulsars in orbit around the central black hole. A deep Galactic Centre pointing at the higher end of S-band could reveal new features building on the recent L-band image from Heywood et al. (2022). Additionally, deep observations help overcome bandwidth depolarization of both compact and diffuse emission that experience extremely large RM ($|{\rm RM}| > 8 \times 10^5$ rad m^{-2}) in the Galactic Centre region. This will reveal a complete and unbiased picture of the magneto-ionic medium around Sgr A*. We refer to this survey as MMGPS-Sgr A* hereafter.

(iv) *Shallow UHF band Galactic Plane Survey (MMGPS-UHF).* This survey covers 400 h of the MMGPS and uses the ultrahigh frequency (UHF) receiver operating between 544 and 1088 MHz at MeerKAT. The UHF band would thus fill in a frequency gap between low frequency (50–150 MHz) and GHz frequencies (1.4 GHz onwards). The primary driver of this survey is the scope to boost pulsar discovery numbers given that pulsars are steep-spectrum sources, i.e., are brighter at lower frequencies. Additionally, a dwell time of 505 s ensures that sensitivity is not compromised to compact binary systems ($P_b > \sim$1.4 h). From the imaging perspective, UHF observations will provide a very wide frequency coverage that will improve the spectral index analysis of the data. This further increases the capability to distinguish between non-thermal and thermal emission of Galactic sources. Finally, The RM studies made at these frequencies will have higher resolution in Faraday space, giving access to a better characterization of the magnetic field structure of background sources used to form the RM grid. Although the expected number of polarized sources will be lower than what is expected at shorter wavelengths due to Faraday depolarization, the UHF observations will allow us to perform depolarization studies of the ISM (e.g. Stuardi et al. 2020).

(v) *Spectral Line Survey (MMGPS-CH/H I/OH).* This survey consists of 55 h of time focusing on observing specific molecular line transitions. Within the 55 h, 40 h are used for specific sources to observe the CH hyperfine transitions (as mentioned in Table 1) using the S-band receiver. Observing the three HFS splitting transitions extends the analysis of CH towards the Southern skies and also complements the observations of the fundamental rotational transitions of CH observed under the SOFIA Legacy program – HyGAL[4] (Jacob et al. 2022). Therefore the main source selection criteria were based on the availability of ancillary data essential for this study, with the HyGAL targets themselves being a subset of the sources identified in the Hi-GAL survey (Elia et al. 2021) with the strongest 160 μm continuum fluxes (>2000 Jy for the inner Galaxy and >1000 Jy for the outer Galaxy). The remaining 15 h will be utilized at L-band to observe (a) H I 21 cm line at 1420 MHz and the (b) OH transitions at 1612, 1665, and 1667 MHz both of which will also complement the other science goals of the SOFIA HyGAL program (Jacob et al. 2022), discussed further in Section 9. A narrow-band mode is available for the L-band aspect of this subsurvey and would use a smaller bandwidth (108 MHz) but higher spectral resolution (32 768 channels). The survey configuration also allows for recording a broader spectral window if needed, thus allowing for simultaneous continuum imaging and pulsar searching.

The survey footprint described above was selected based on the following constraints.

(i) The total possible survey footprint at each frequency is constrained by the allocated time, integration length, and the total number of synthesized beams that can tile a pointing. We have also assumed a 90 per cent efficiency for the allocated time to accommodate the time required for flux and phase calibration, slewing, and failures.

(ii) The upper longitude limits for the subsurveys are restricted by the declination limits of the most sensitive telescopes in the Northern hemisphere that have previously conducted or are conducting Galactic plane surveys in these frequency bands. For MMGPS-L, the declination limit of the Green Bank Telescope (GBT) ($\delta > -46^\circ$) and Very Large Array ($\delta > -40^\circ$) is imposed. Although surveys with the GMRT can achieve lower declination limits, the GMRT survey region (see Bhattacharyya et al. 2016) has minimal overlap with the MMGPS-UHF survey and is at a different observing frequency (322 MHz versus 816 MHz). Similarly, for MMGPS-S, the upper longitude is limited to avoid overlap with the FAST sky ($-15^\circ < \delta < 65^\circ$).

(iii) The lower limits on the longitude are survey dependent. For MMGPS-L, we have chosen a region to maximize the predicted yield of pulsar discoveries with the caveat of ensuring that certain targeted regions for other science cases fall within the specified boundary. This includes spiral arms like the Carina arm for extreme RM measurements (as mentioned in Section 2.2). On the other hand, the MMGPS-S has the same lower longitude limit to ensure maximum overlap between L-band and S-band regions. A higher overlap proves beneficial for stacking spectral lines across bands to boost sensitivity. It also provides complementary RM grids and enables spectral index deduction for a larger number of sources. Further details on other constraints for executing commensal observations are explained in Section 7.

(iv) Extensive testing revealed that atomic and molecular spectroscopy at adequate spectral resolution is not feasible over the full survey range due to high data rates in the MeerKAT network proving to be a bottleneck. This led to carving out a dedicated subsurvey within the time budget to specifically administer the scientific needs of spectral line science (as described in Section 2.3).

(v) We also ensured that a significant fraction of time within the 3000 h budget can be spent on following up interesting discoveries. Apart from the 2835 h spent observing with the subsurveys, we currently have 175 h allocated for follow-up.

4 INSTRUMENTATION

4.1 Frontend

The MeerKAT telescope consists of a mixture of commercial off-the-shelf and state-of-the-art custom instrumentation offering high-fidelity data recording across a wide range of frequencies (Camilo et al. 2018; Jonas & MeerKAT Team 2018). The antennas are currently equipped with dual (linearly) polarized L-band (856–1712 MHz), UHF band (544–1088 MHz), and S-band receivers (1.75–3.5 GHz) that are installed at the secondary focus of the dish (Camilo et al. 2018). The MMGPS utilizes each of these receivers.

4.1.1 L-band receiver

The L-band receiver operates between 856 and 1712 MHz, centred at 1284 MHz. Although the L-band receiver provides a total bandwidth of 856 MHz, several parts of the bandpass are affected by known radio frequency interference (RFI) signals leading to an effective bandwidth of 684 MHz. The system temperature of the receiver alone is 18 K (Bailes et al. 2020) and an extra contribution ranging from 4 to 7 K is added from the atmosphere and ground spillover. The system equivalent flux density (SEFD) is as low as 400 Jy for an individual dish at the centre of the band.[5]

[4]HyGAL is a spectroscopic survey that aims to characterize the diffuse Galactic ISM through observations of six key hydrides (molecules of the form XH_n or XH_n^+ including ArH^+, H_2O^+, OH^+, CH, OH, and SH) toward 25 Galactic background continuum sources.

[5]https://skaafrica.atlassian.net/rest/servicedesk/knowledgebase/latest/articles/view/277315585

4.1.2 S-band receiver

The S-band receiver system has been designed and built by the MPIfR and is intended to be complementary to the existing L-band and UHF receivers (Kramer et al. 2018). The frequency coverage of the receiver ranges from 1.75 to 3.5 GHz with a maximum digitized bandwidth of 1.75 GHz but a usable bandwidth of 875 MHz. The selected observing band can be centred at five different centre frequencies (2187.50 (S0), 2406.25 (S1), 2625.00 (S2), 2843.75 (S3), and 3062.5 (S4) MHz; Barr 2018). The development of this receiver was motivated by different science cases (as explained in detail in Section 2). The S-band receivers are installed on all 64 antennas. Similar to the other receivers, the S-band receiver is equipped with a cross-dipole dual-polarization receptor. The system temperature is 22 K with the SEFD of ∼400–450 Jy per individual receiver (Wucknitz et al., in preparation).

4.1.3 UHF-band receiver

The ultrahigh frequency (UHF) receiver operates between 544 and 1088 MHz. Unlike the L-band, the bandwidth is not significantly impacted due to RFI making most of the band usable (∼90 per cent). The system temperature of the receiver goes down to 20 K at the middle of the band with atmospheric and ground spillover contributing an extra 6–8 K. The average SEFD across the band is ∼550 Jy per antenna.

4.2 Backend

For all receivers, the induced voltages are amplified, filtered, and directly sampled at the focus of each dish. The observatory clock is a maser with a GPS receiver for universal time tracking. A time and frequency reference (TFR) subsystem is used to maintain the time standard via a 1 pulse per second (1PPS) and 100 MHz clock distribution. The digitized data streams are packetized and transmitted over a 40-GbE correlator/beamformer (CBF) network to the Karoo Data Rack Area (KDRA), a data centre located in the Karoo Array Processor Building (Camilo et al. 2018; Jonas & MeerKAT Team 2018). The digitized streams then enter the CBF switch. The CBF consists of several systems responsible for producing different data products catering to various MeerKAT science cases. Data products from these systems are transmitted back into the CBF network where any other system can capture this stream and process it further. The MeerKAT CBF network uses multicast ethernet and a folded-Clos topology to enable any-to-any communication between attached instruments (Slabber et al. 2018). This way, data published by one instrument can be subscribed to by another. The network can be made compatible with hardware supplied by external collaborators to produce data products pertaining to their science case. These are termed as User Supplied Equipment (USE). A detailed description of the MeerKAT network can be found in Slabber et al. (2018). Similarly, a comprehensive explanation of the correlator/beamformer apparatus at MeerKAT is given in van der Byl et al. (2022). For MMGPS, there are four systems of interest. Two of these systems are provided by the South African Radio Astronomy Observatory (SARAO) and used for standard imaging observations. These are as follows.

(i) *F-Engines.* The CBF F-engines channelize the digitized voltages from the MeerKAT antennas using a 16-tap polyphase filter with the filter coefficients weighted by a Hann window (e.g. Bailes et al. 2020). The system is implemented on the Square Kilometre Array Reconfigurable Application Board (SKARAB),[6] with several channelization modes being provided over both full (wide-band) and reduced (narrow-band) bandwidths. The imaging and time-domain science cases of the MMGPS use a 4096-channel (hereafter 4k) mode of the wide-band F-engines to achieve ≈210 kHz frequency resolution. Our spectral line science case requires the higher frequency resolution provided by a 32 768-channel (hereafter 32k) mode applied by the narrow-band F-engines over a ≈108 MHz band, providing ≈3.2 kHz resolution.

(ii) *X-engines.* This CBF X-engines are responsible for cross-correlating the channelized voltages streams output formed by the F-engines. They support all modes of the F-engines, with wide- and narrow-band capabilities that can be run simultaneously. The visibilities produced by the X-engines are transmitted through the CBF network to the Science Data Processor (SDP) system that performs quality analysis and quick-look imaging and archiving the raw visibilities for later use. These data products are used by both the spectral line and imaging science cases of the MMGPS.

A high-level view of the data flow through the CBF network is shown in Fig. 2. While the F- and X-engines can produce data products needed for imaging and spectral line studies, there is a need for specialized hardware that is capable of producing beamformed data products useful for pulsar searches. While MeerKAT offers a system capable of producing a tied-array beam (known as B-engines; see Bailes et al. 2020), the number of beams that can be produced simultaneously is limited (maximum of four). This limits the field of view to few tens of arcseconds, making it infeasible to cover a large enough area for pulsar searching within the time budget of the survey. There is thus a need to produce hundreds of synthesized beams in real-time. This enables a large fraction of the primary beam to be tiled, thus ensuring the time constraint is met without major gaps in the sensitivity. Besides this, new discoveries made in these synthesized beams would already have a tight constraint on the position, thus reducing the time needed for generating a robust timing model of the pulsar (Bezuidenhout et al. 2023). Furthermore, a set-up with multiple beams also provides scope for developing RFI mitigation algorithms based on spatial filtering and candidate classification (e.g. Kocz, Briggs & Reynolds 2010; Kocz et al. 2012).

Besides the S-band receivers, MPIfR has thus also invested in two systems that have been integrated into the MeerKAT network primarily for pulsar and transient searching (Barr 2018; Kramer et al. 2018). These systems have already been used for the TRAPUM project (Stappers & Kramer 2018) and played a pivotal role in making numerous discoveries. The systems are described below.

(i) *Filterbanking beamformer user supplied equipment (FBFUSE).* The FBFUSE cluster is a high-performance mutlibeam beamformer capable of ingesting the full data rate output from the F-engine wide machines (up to 1.8 Tb s^{-1} for the entire cluster) and perform multiple beamforming operations in real-time. Calculation of the necessary tiling is done using the MOSAIC[7] software stack (Chen et al. 2021). A GPU-based processing pipeline produces filterbank data products on which pulsar search pipelines can be run. FBFUSE also consists of a transient buffer that is able to store 30 s worth of base-band data from the F-engines. This can be used to produce visibilities and beamformed products offline making it suitable for following up on triggers generated from fast transient

[6] https://casper.ssl.berkeley.edu/wiki/SKARAB
[7] https://github.com/wchenastro/Mosaic

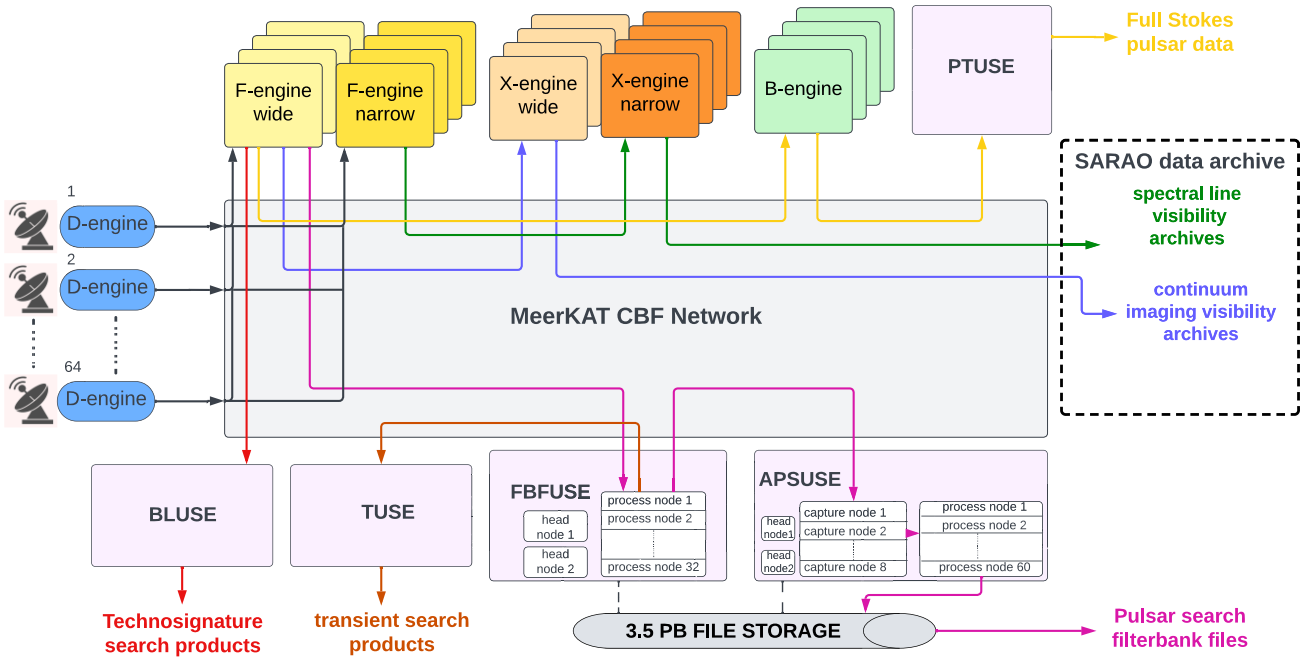

Figure 2. Schematic representation of the data flow from the MeerKAT receivers to the final data products for each of the science cases (pulsar, continuum, and spectral line). Once the data are directly digitized by the D-engines at the receiver, the data flow through different backends. The different colours represent different processes needed to reach the eventual data product. The MeerKAT CBF network is multicast allowing for different backends to subscribe to each other. Four backends are external to SARAO that subscribe to MeerKAT CBF network to produce the necessary data products. PTUSE subscribes to the B-engines. FBFUSE subscribes to the F-engine wide system. APSUSE and TUSE subscribe to the output from FBFUSE. BLUSE subscribes to the F-engines directly.

sources discovered from the MeerTRAP project (Rajwade et al. 2020). The cluster contains two head nodes (RAM of 32 GB), 32 processing nodes (with a RAM of 384 GB), and a total of 64 GPUs for this purpose. More details about beamforming with FBFUSE can be found in Barr (2018) and Voraganti Padmanabh (2021).

(ii) *Accelerated pulsar search user supplied equipment (APSUSE).* APSUSE is a high performance cluster that captures and stores the filterbank data products (input data rates of up to 280 Gb s^{-1}) generated from FBFUSE. FBFUSE and APSUSE share a common file storage of 3.5 PB on a BEEGFS[8] distributed file system. This system is capable of producing read/write speeds of up to 50 GB s^{-1} and consists of two head nodes, eight capture nodes (to capture data from FBFUSE), and 60 processing nodes (to deploy the pulsar search pipeline) enabled with 120 GPUs in total (2 GeForce GTX 1080 Ti GPUs per node). The pulsar search pipeline deployed on APSUSE is described in detail in Section 6. More information on the specifications of APSUSE can be found in Barr (2018) and Voraganti Padmanabh (2021).

5 OBSERVATIONAL SET-UP

MMGPS observations are conducted in 4–8 h blocks with pointings having an elevation limit of 50° for pointings (see Section 7 for reasoning). The MeerKAT configuration authority (CA) serves as a mediator for communication between the user and telescope control. More details on the control and observation monitoring system at MeerKAT can be found in Marais (2015).

For MMGPS-L, the complex visibility data products for continuum science cases are recorded in the so-called 4K spectral mode, which results in a channel frequency resolution of 208.9 kHz. Data from all 64 MeerKAT antennas are used to generate the visibility data. To be able to calibrate the visibility data, we include scans on flux density, polarization angle, and phase reference calibrators in each observing run. The bright extragalactic sources J1939−6342 and J0408−658 are used as flux density calibrators, and 3C 138 and 3C 286 are observed to facilitate polarization calibration. We assume the Stevens–Reynolds 2016 model for J1939−6342 (Partridge et al. 2016), and use the Perley & Butler (2013) models for 3C 138 and 3C 286. J0408−658 is a non-standard calibrator, for which we have assumed a model provided by SARAO[9] phase reference calibrators is observed with a cadence of 40 min (once after four target pointing scans). The phase calibrators were chosen from a set of sources that have been tested to produce stable phase solutions in the course of the MeerKAT commissioning effort.

Once an observation begins, the configuration parameters enable different hardware backends to be triggered for data recording. From the pulsar search side, FBFUSE beamforms the incoming data produced from the F-engines and streams it back to the MeerKAT network to be retrieved by APSUSE to be written out as filterbank format files on the file system. The filterbank files generated during calibrator scans are deleted post-observation due to storage constraints. On the imaging and spectral line side, the F-engine output is relayed to the X-engines and the correlated FX products (or visibilities) are stored as data archives that can be downloaded via a portal. This continues to operate throughout the entire observation. The observations and instrument status are

[8]https://www.beegfs.io/c/

[9]For more details, see https://skaafrica.atlassian.net/wiki/spaces/ESDKB/pages/1481408634/Flux+and+bandpass+calibration#J0408-6545

monitored via a portal to the control and monitoring set-up for MeerKAT. Additional monitoring of server loads is done via an open source analytics and interactive visualization web application known as GRAFANA.[10]

6 PROCESSING

This section describes the different processing pipelines implemented for the respective science cases of the MMGPS. As such, we describe the pulsar search and continuum imaging and spectral line processing pipelines in the following subsections.

6.1 Pulsar search processing

6.1.1 Pipeline workflow

In order to maintain a constant rate of observation within the limited storage capacity, processing the data in quasi-real-time is necessary. For tracking and processing data efficiently on the cluster, we have implemented a scheme using open source tools ensuring flexibility in implementing and improving the pipeline with time. It also takes care that the APSUSE cluster is used optimally in terms of management of computing resources. Although this scheme is explained in Voraganti Padmanabh (2021), several changes have been made to the set-up since. These changes have been important not only for MMGPS, but also for TRAPUM related pulsar search processing. We hence describe the latest set-up in detail below.

Jobs are deployed on the APSUSE cluster via microservices launched using DOCKER[11] containers. Containerized service provisioning is orchestrated by KUBERNETES,[12] thus integrating multiple nodes of the cluster for one processing unit chain. The input parameters to the containers running these jobs are brokered by a MONGODB[13] instance. Additionally, a MySQL[14] data base is running as a service enabling efficient tracking of input and output data products from the deployed jobs.

Additionally, an internal web page has been built on the foundation of the MySQL data base and maintained on the head node of the FBFUSE cluster. This web page provides an interface to make specific processing requests. Once a user sends in a processing request, the information is relayed as input parameters to the pipelines executable. The web page is automatically updated with the latest state of the processing that was launched by the user. Once processing is complete, relevant details like the path to the data products are displayed for users to follow up on. The overall infrastructure ensures flexibility in integrating any new pipeline into the system. Scripts that help in deploying and scaling jobs across the APSUSE cluster are regularly maintained in a repository.

6.1.2 Processing pipelines

The different processing pipelines currently used for pulsar searching and their specific roles are briefly discussed below.

(i) *Acceleration searching.* We use PEASOUP,[15] a GPU implementation of a time-domain resampling (e.g. Lorimer & Kramer 2004) acceleration search pipeline (Morello et al. 2019; Barr 2020). This implies that the processing time reduces compared to CPU-based pipelines but also ensuring that the survey is sensitive to detect a range of binary pulsars. Dedispersion across different DM trials were conducted using the DEDISP library (Barsdell et al. 2012). An acceleration range can be specified with an acceleration trial step size that is set based on a threshold tolerance value. This ensured that the contribution due to smearing between trials is not more than a fixed fraction of the smearing due to a finite sampling time and intrachannel dispersion (see Morello et al. 2019, for more details). Post-resampling, PEASOUP also contains routines for red-noise removal and incoherent harmonic summing. Prior to implementing these searches, the filterbank file undergoes cleaning to mitigate effects due to RFI. Several techniques and packages have been tested including IQRM (Morello, Rajwade & Stappers 2022) and RFIFIND from PRESTO (Ransom 2011). We currently use FILTOOL from the PULSARX[16] package. This algorithm offers a variety of different filters to detect outliers in the time and frequency domain. Signals detected above a certain threshold are retained for the next step of candidate filtering.

(ii) *Multibeam candidate filtering.* In order to reduce the number of candidates across different tied array beams, we apply spatial filtering techniques to distinguish RFI signals from potential pulsar signals. This is a two-stage filtering process. First, known RFI signals are cross-matched against the candidates as a first level filter. Secondly, multibeam coincidencing is used, where the candidates based on common periodic signals are clustered initially. A fit is then applied to evaluate how the signal strength varies across the spatial dimension for all the clustered signals. The clustering also takes into account the acceleration value and ensures that differences in acceleration are also translated to differences in spin period while applying a threshold for clustering together similar candidates. RFI signals would tend to be detected across several beams showing a relatively flat profile across the spatial dimension. However, true pulsar signals and related harmonics would be detected in a couple of beams at most and would show an exponential drop in signal-to-noise ratio (S/N) away from the true position. Mathematically, we model the drop in S/N with an exponential function and a threshold is applied on the rate at which the S/N drops from the brightest detection of a candidate. This helps distinguishing RFI from potential pulsar candidates. Further details on this implementation can be found in the CANDIDATE_FILTER[17] repository made publicly available. This multibeam filtering procedure reduces the number of candidates by a factor of 3–4 typically down to a few thousand candidates per pointing.

(iii) *Folding and post-folding candidate sifting.* The remaining candidates are phase-coherently folded from the time series using the spin period, DM, and acceleration parameters that are obtained from the PEASOUP pipeline. This is done using the PSRFOLD_FIL routine from the PULSARX[18] package. This routine is efficient in memory management and processing speed, thus ensuring that this step in the search process does not prove to be a major bottleneck when scaled. The final data product is a folded archive file that can be visualized and inspected using the PSRCHIVE[19] package. These archives are then scored against a convolutional neural net-based machine learning

[10] https://grafana.com/
[11] https://www.docker.com/
[12] https://kubernetes.io/
[13] https://www.mongodb.com/
[14] https://www.mysql.com/
[15] https://github.com/ewanbarr/peasoup
[16] https://github.com/ypmen/PulsarX
[17] https://github.com/prajwalvp/candidate_filter which is a fork of https://github.com/larskuenkel/candidate_filter
[18] https://github.com/ypmen/PulsarX
[19] https://psrchive.sourceforge.net/

classifier known as PICS (Zhu et al. 2014). The trained models include data from the PALFA survey (Cordes et al. 2006) and a new model generated from retraining the classifier using candidates generated from the TRAPUM survey. The score generated by the models range from 0 to 1 where 1 indicates a high likelihood for the candidate to be a pulsar. Candidates above a certain PICS score and S/N threshold are retained for human inspection. The retained candidates are typically between 100 and 200 per pointing.

6.1.3 *Candidate viewing*

A specialized candidate viewing tool termed CANDYJAR[20] has been developed to provide a user friendly interface for classifying candidates inspected by eye. The tool displays a diagnostic plot generated by the folding pipeline and candidate metadata and known pulsars in the field to help make decisions on the type of candidate that is seen. The tool provides options to mark the candidate as a known pulsar, RFI, noise, or a potential new pulsar candidate. The human labels are recorded in order to use the information for training and retraining supervised learning-based classifiers in the future.

6.1.4 *Current survey status and processing strategy*

We first initiated the MMGPS-L survey with regular observations conducted since beginning of 2021 February. As of 2022 December, we have completed the entire MMGPS-L survey amounting to a total of 4140 pointings. While the initial calculations assumed 960 beams could tile the primary beam, recording this many beams for APSUSE during initial testing proved to be a bottleneck for real-time operations. Besides this, maintaining a steady processing rate per week also proved to be computationally expensive. For this reason, the number of tied array beams recorded was reduced to 480 tied-array beams (a factor of 2 lower). The sampling time was set to 153 μs with 2048 frequency channels across 856 MHz bandwidth centred at 1284 MHz. In order to ensure the right balance between a reasonable sensitivity and improved coverage, we ensured that not more than 40 antennas are used to produce the tied array beams (Chen et al. 2021). Moreover, these antennas are from the inner core (within a 1 km diameter) of the MeerKAT array. This way the synthesized beams are wider than using the full array also ensuring no 'holes' in the gain across the surveyed patch of sky.

The numbers chosen for the DM and acceleration ranges of the search trials were predominantly based on processing time constraints. Similar constraints have been applied at different steps of the processing, the details of which are explained below. First, we assumed that the processing speed on APSUSE is eight times slower than real-time. On one hand, this ensures that the robustness of the pipelines is not compromised while focusing on enhanced processing speed alone. On the other hand, it also ensures that new observations can be scheduled on a weekly cadence given the constraints on disc storage space on APSUSE.

We chose a DM range of 0–3000 pc cm^{-3} with variable step sizes as generated by DDPLAN.PY from PRESTO (Ransom 2011). The acceleration range for PEASOUP was set to −50 to 50 ms^{-2} with a default acceleration tolerance of 10 per cent. The number of candidates per beam produced from PEASOUP was limited to 1000 and the fast Fourier transform (FFT) S/N threshold was set to 8.5. Although the false alarm statistics (see e.g. Lorimer & Kramer 2004) gives an S/N threshold of 10, we applied a conservative threshold down to 8.5. The candidates generated from each of the 481 beams were put through the CANDIDATE_FILTER spatial filter before folding. Besides this, an S/N threshold of 9.5 is chosen as the cut-off to select candidates before filtering.[21] The motivation behind choosing 9.5 than 8.5 for the S/N threshold was to reduce the time required for filtering and subsequent folding by a factor of at least 2. Furthermore, we removed candidates below a DM of 2 pc cm^{-3} given that such candidates are most likely RFI. Post-candidate filtering, an upper limit of 50 candidates per beam was set for the folding. This is a reasonable cap limit given that the candidates per beam produced from the candidate filtering pipeline do not exceed 50 for 99 per cent of all the beams. We selected candidates that score above 0.1 on the PICS ML classifier and a folded S/N above 7.0 for candidate viewing. This conservative approach on the classifier was chosen to avoid missing weak potential candidates that have scored poorly due to different statistics in comparison with the original training set used for generating the PICS model.

The CANDYJAR tool along with a software suite of candidate data extraction scripts[22] enabled quick viewing and classification of candidates. Beams corresponding to interesting candidates and known pulsars were retained for further inspection. Besides this, beams with promising candidates that cross-match with potential unassociated *Fermi* sources that show gamma-ray pulsar-like properties (e.g. Saz Parkinson et al. 2016) were also retained for further analysis. Once the beams were analysed, those ones that are not flagged for retention were deleted.

Once a convincing candidate was seen, a series of steps were undertaken to confirm and better understand the properties of the potential discovery. These are summarized in the steps below.

(i) The candidate parameters were used to refold the neighbouring beams with respect to the reference beam where the candidate was found. Detection of the same candidate in just a few neighbouring beams with a reduced S/N indicates that the source is far-field rather than terrestrial. This provided a quick way to confirm candidates without scheduling a separate observation.

(ii) Confirmation observations for convincing candidates were scheduled within the allocated slots for MMGPS observations. A redetection in this observation confirmed the candidate as a new discovery.

(iii) The multibeam capability of the survey was also used for constraining the position of the pulsar. This is particularly useful for follow-up timing studies given that the spin period derivative and position are covariant for nearly a year of timing baseline. In order to further refine the pulsar coordinates, the first confirmation observation of a discovery was scheduled such that 12 beams encircled the central reference beam (pointed at the known coordinates) with a beam overlap factor increased to 0.9. The candidate parameters were then used to refold the beams and estimate the S/N in each beam. This information along with the synthesized beam obtained from MOSAIC (Chen et al. 2021) was used as an input to SEEKAT,[23] a program that calculates localization contours where the ratio of point spread functions (PSFs) are matched to the ratio of S/N detections. The localization algorithm is described thoroughly in Bezuidenhout et al. (2023).

[20] https://github.com/vivekvenkris/CandyJar

[21] The value of 9.5 was chosen here from processing speed constraints after extensive benchmarking. It is also roughly similar to the value based on the false alarm probability.

[22] https://github.com/prajwalvp/mgps_utils

[23] https://github.com/BezuidenhoutMC/SeeKAT

(iv) Depending on the type of discovery, the strategy for further follow-up of the discoveries varied. Binary pulsar discoveries were monitored regularly (initially with a pseudo-log spacing of observations followed by a weekly/monthly cadence) in order to obtain an orbital solution and finally a phase coherent timing solution. The orbital motion was fit for using the PYTHON version of FITORBIT.[24] However, isolated pulsars were monitored once in several months in order to eventually obtain an estimate on the period derivative. The now public PTUSE backend (Bailes et al. 2020) was used to follow-up and produce full Stokes archive files (enabling polarization studies) and PSRFITS formatted search mode files that were coherently dedispersed at the DM of the discovery. Apart from this, some of the discoveries are also being followed up with the ultra-wide-band receiver (UWL) at the Parkes radio telescope and Northern telescopes like the 100-m Effelsberg radio telescope in collaboration with the TRAPUM Follow-up Working Group.

6.2 Image processing

As mentioned in Section 4.2, the FX-correlated data products are recorded as complex visibility data for continuum and spectral line imaging purposes. The raw visibility products were stored on SARAO tape archive[25] for long-term storage. The data were calibrated and imaged at MPIfR using a custom pipeline that was built in-house.

We calibrated and image our visibility data following standard prescription using the Common Astronomy Software Application (CASA version 6.4; McMullin et al. 2007) and WSCLEAN (version 3.1; Offringa et al. 2014; Offringa & Smirnov 2017) software packages. Our calibration and imaging pipeline is functionally similar to other publicly available MeerKAT pipelines like the IDIA pipeline[26] and the CARACAL pipeline.[27] In the remainder of this section, we briefly explain the various steps in our calibration and imaging scheme.

6.2.1 *Flagging and calibration*

We first pre-flagged the visibility data to flag autocorrelation data and time slots affected by shadowing effects between antennas. We then used the TRICOLOUR[28] software package to apply a static mask that flags all the frequency channels that are known to be affected by persistent RFI. At L-band, edge channels outside the 900–1670 MHz frequency range were also flagged.

The pre-flagged visibility data were then calibrated following an iterative process that progressively flags any residual time-dependent RFI.

(i) The pre-flagged visibility data were divided into 16 spectral windows using the `mstransform` task in CASA.

(ii) We derived delay, bandpass, complex gain, and leakage solutions using the unpolarized primary flux density calibrator. We applied the derived calibration solutions to the primary calibrator, subtracted the known model of the calibrator from the calibrated visibility data, and flagged the residual data for RFI using the RFlag and TFCrop algorithms in CASA. We then discarded the old solutions and rederived them from the RFI-flagged primary calibrator.

(iii) Next, we derived an intrinsic model for the secondary phase reference calibrator by deriving the complex gain corrections from the secondary and then scaling them using the gain corrections from the primary flux density calibrator. We then applied the scaled complex gain corrections from the secondary and the delay and bandpass corrections from the primary to the secondary calibrator. Following the same procedure mentioned in step (ii), we flagged the secondary calibrator for any residual RFI. Finally, we derived the scaled complex gain solutions from the secondary.

(iv) Finally, we applied the various solutions derived from the primary and secondary calibrators to the target scans. We once again flagged the calibrated target visibility data for any remaining RFI.

The visibilities flagged in this step are ignored in all the subsequent processing steps. Flagging the frequency channels with known RFI reduces the total useful bandwidth. However, it does not have a significant impact on the synthesized beam of the broad-band data.

Note that the development version of our pipeline supports full polarization calibration, which is currently being validated. A detailed description of the full polarization calibration scheme and results from this analysis will be described in a future publication.

6.2.2 *Imaging*

We imaged each target pointing separately using WSCLEAN. The visibilities data were Fourier transformed using the fast W-gridder algorithm (Arras et al. 2021; Ye et al. 2022) using a Briggs visibility weighting scheme (Briggs 1995) with the `robust` parameter set to −0.75. Since MeerKAT has a dense core of antennas, a slightly uniform visibility weighting scheme is needed to suppress the sidelobes of the synthesized beam. We complemented the uniform visibility weighting scheme with an appropriate Gaussian tapering to better recover diffuse emission in pointings with strong large-scale Galactic emission. The dirty images were deconvolved using the multiscale, wide-band deconvolution algorithm available in WSCLEAN. The deconvolution process was steered using the automasking and autothresholding algorithms available in WSCLEAN. For some pointings, the automatically generated mask did not encapsulate all the diffuse emission within the field of view. In such cases, we manually generated a mask using the BREIZORRO[29] software package.

Finally, we applied an image-based primary beam correction to each image with a beam response generated using the KATBEAM[30] software package. The primary beam corrected images were stitched together, following a linear mosaicing strategy, to generate mosaiced images of fields of interest.

Our pipeline does not yet perform automated self-calibration to improve the calibration solutions derived using the secondary calibrator. Inadequate phase calibration resulted in artefacts in the final target images. After visual inspection, target fields judged to suffer from this issue were improved by manually applying a few iteration of phase-only self-calibration. We aim to implement automated self-calibration in the future versions of our pipeline.

6.3 Spectral lines

As the continuum reduction pipeline included all necessary steps for spectral line reduction, the reduction of the dedicated observations with the narrow-band spectral line correlator mode as part

[24] https://github.com/gdesvignes/pyfitorbit
[25] https://archive.sarao.ac.za/
[26] https://github.com/idia-astro/pipelines
[27] https://github.com/caracal-pipeline/caracal
[28] https://github.com/ratt-ru/tricolour
[29] https://github.com/ratt-ru/breizorro
[30] https://github.com/ska-sa/katbeam

of MMGPS-CH/H I/OH followed closely the steps described in Section 6.2.1. The smaller data volume allowed us to adapt the calibration individually. We did not apply any averaging and restricted automatic flagging during calibration to the calibrators alone. The calibration solutions and data were inspected visually. After subtracting the continuum emission directly from the visibilities with the CASA task `uvcontsub`, we imaged and deconvolved the spectral lines with the task `tclean` in CASA. To obtain accurate continuum measurements, we separately imaged the line-free channels around each transition as Stokes I MFS images with `tclean`.

7 COMMENSAL STRATEGY

A key feature of the MMGPS is its nature of being a fully commensal undertaking wherein the same telescope time is used to pursue multiple science cases. Below we discuss the observing strategies that have been implemented to support commensality.

7.1 Other commensal backends

Apart from the instrumentation specified in Section 4, there are other backends that operate during MMGPS observations. First, the Transient User Supplied Equipment (TUSE) backend operated by the MeerTRAP Collaboration (Rajwade et al. 2020)[31] operates in commensal mode with the majority of MeerKAT observations including MMGPS. This backend enables the real-time detection of fast radio transients including FRBs. A single pulse search pipeline searches DMs up to 5000 pc cm^{-3}. Candidates are then sifted using a deep learning-based classifier FETCH (Agarwal et al. 2020). Candidates that are likely real result in a trigger being sent to the FBFUSE transient buffers to capture the corresponding channelized voltages to disc. These data allow for precise localization of the source of any transient signal. More details about the TUSE search set-up can be found in Rajwade et al. (2020). Secondly, discoveries from MMGPS are followed up commensally with PTUSE in order to obtain coherently dedispersed full Stokes pulse profiles (as mentioned earlier in Section 6.1.4). Recently, the Breakthrough Listen Use Supplied Equipment (BLUSE) system has begun operations with the aim of finding technosignatures in data indicative of extraterrestrial life (Czech et al. 2021). Similar to TUSE, BLUSE also operates as a separate commensal backend.

7.2 Survey grid scheme

The survey grid scheme uses hexagonal packing with the minimum separation between pointing centres (henceforth the survey beam radius) set to FWHM/$\sqrt{5}$, where FWHM is the full width at half-maximum of the primary beam. Although a value of FWHM/2 suffices for reducing the variance of the gain across pointings for imaging calibration purposes, more tied-array beams would have been needed to populate the survey beam area. We thus increased the overlap factor without compromising on the imaging needs, thus ensuring maximum efficiency and highest pulsar discovery potential.

7.3 Survey coverage optimization

Before commencing the survey, we had conducted tests to find the tiling configuration and elevation that results in the highest average gain across the field of view. We simulated a pointing with 480 beams where each beam was modelled as an ellipse with a two-dimensional Gaussian profile. Multiple tilings were produced by varying two parameters namely, the elevation (10°–90°) and overlap factor between beams (0.05–0.95). Fig. 3 summarizes the findings of this simulation. It shows a heat map of the coverage across a hexagonal patch of sky whose edge length is the survey beam radius. Given that blocks allocated for MMGPS typically last 4–8 h, a range of elevations is covered in this process. Keeping this in mind, an overlap factor of 0.5 provides a higher average gain at all elevations. This corresponds to a minimum fractional gain (i.e. the fraction of gain at boresight) of 0.5 for 78 per cent of the field of view. Furthermore, the elevation profile shows that elevations above 50° reduce the coverage above half-power fractional gain to below 70 per cent. For this reason, we implemented a cap of 50° as the elevation limit while scheduling observing blocks for MMGPS-L. Keeping in mind the commensal nature of the survey, we also try to schedule observations above a lower limit elevation of 20° when possible, to reducing excess spillover.

For bulk of the second half of the MMGPS-L survey blocks, a new tiling configuration was implemented for the tied array beams. Earlier, the tied array beams were placed with an overlap factor of 0.5 within a circular region whose radius was the survey beam radius. The latest scheme implemented a tiling configuration where the tiling grids are themselves shaped as hexagons. This way, there are no obvious gaps in the area between pointings. Fig. 4 demonstrates an example of the current scheme. The plan is to use the current scheme for future MMGPS-S observations as well.

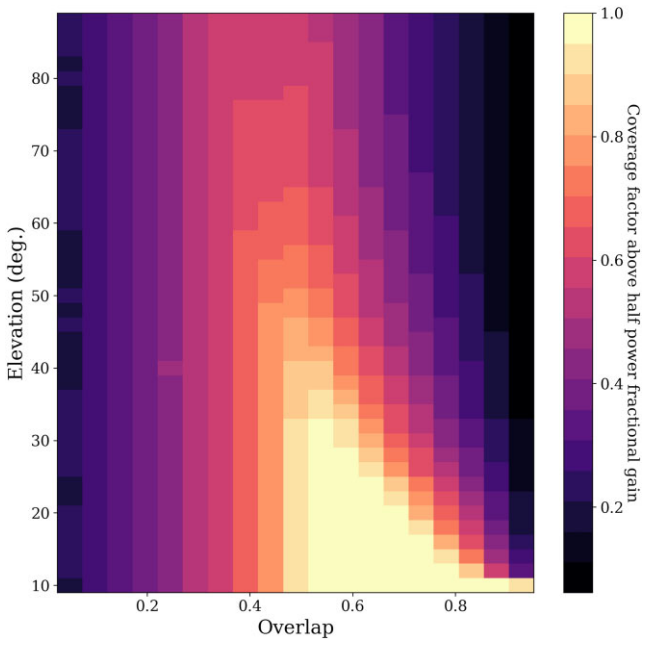

Figure 3. The simulated coverage for a minimum fractional gain of 0.5 (i.e. half-power) as a function of the overlap factor between tied-array beams and the telescope elevation for a pilot survey pointing chosen at random. The coverage is dependent on the sensitivity profile within the beam tiling as well the area covered by the tied-array beams as a fraction of the survey beam area. Low overlap factors increase the spacing between the beams and in turn increase the overall coverage. However, they decrease the achievable sensitivity between beams, thus reducing the overall gain. High overlap factors decrease the coverage but provide a more uniform sensitivity between beams within the tiling. High and low elevation tends to shrink and elongate the size of the beam, respectively.

[31] https://www.meertrap.org/

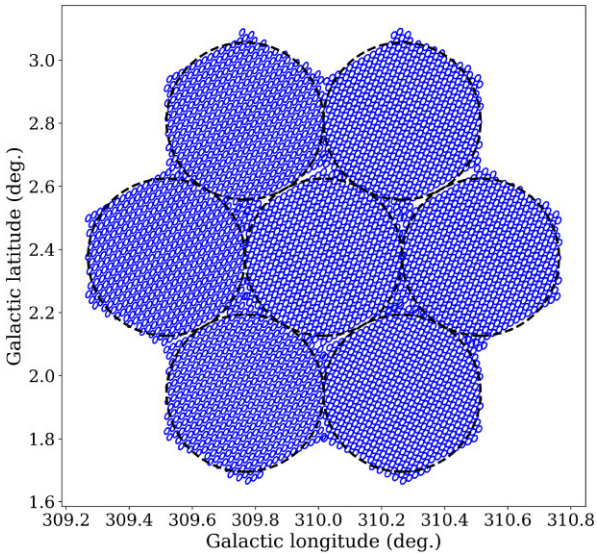

Figure 4. Representation of the new tiling scheme of synthesized beams recorded for pulsar searching implemented for the MMGPS-L survey. The central positions of the chosen grid of pointings are separated by FWHM/$\sqrt{5}$ of the primary beam (used as the radius for the black dashed circles). The synthesized beams (marked in blue) are placed farther apart with an overlap factor averaging 0.3 in a hexagonal tiling such that the survey beam circle touches all the sides of the hexagon. This ensures a near uniform coverage.

8 PULSAR DISCOVERIES

The MMGPS-L survey has so far yielded 78 discoveries[32] at the time of writing including 16 MSPs ($P < 20$ ms) and seven potentially mildly recycled binary pulsars ($20 < P < 100$ ms). The initial set of parameters for the new pulsar discoveries, including the best localized positions and whether they are binary systems, is summarized in Table 3. A collage of pulse profiles of all the discoveries is provided as Fig. 5. Timing solutions for the discoveries will be published in future papers. Here, we briefly discuss properties of some MMGPS pulsar discoveries categorized based on spin period. Note that all companion mass estimates presented for binary systems assume a pulsar mass of 1.35 $M_\odot$.

8.1 Millisecond pulsars

Of the 16 millisecond pulsars (MSPs) discovered by the survey so far, 10 are confirmed to be in binary systems. We discuss some highlight discoveries below.

8.1.1 PSR J1306−6043

PSR J1306−6043 was the first pulsar discovery of the MMGPS. It was initially discovered as a 19 S/N candidate. The pulsar has a spin period of 5.67 ms and a DM of 67.10 pc cm^{-3}. The source was also weakly detected in a refined search conducted via a reprocessing of data from the HTRU South low-latitude survey (Keith et al. 2010). Follow-up observations revealed the barycentric spin period to be changing, hence suggesting a binary companion to the pulsar. Since then, the pulsar has been monitored with a weekly to monthly cadence for a year with MeerKAT and on a monthly basis with the Parkes radio telescope. We obtained a phase-connected timing solution for approximately 1.3 yr of data using the DRACULA algorithm (Freire & Ridolfi 2018). The solution revealed a circular orbit with an orbital period (P_b) $\sim$ 86 d and projected semimajor axis (x) $= 40$ lt-s with a minimum companion mass of 0.29 $M_\odot$. This places it as a potential MSP helium white dwarf (HeWD) system. The pulsar was found to be within the positional uncertainty of a *Fermi* source 4FGL J1306.3−6043. The radio solution enabled a detection of this pulsar in gamma-rays using the *Fermi* Large Area Telescope data. A detailed description of the radio and gamma-ray analysis will presented in a future publication.

8.1.2 PSR J1708−4843

PSR J1708−4843 is a 16.66 ms binary pulsar with a low DM of 28.7 pc cm^{-3}. It suffers from significant scintillation, resulting in a highly variable S/N per epoch. We have obtained a phase-connected timing solution spanning roughly 200 d revealing a circular orbit of 13.06 h. With a relatively slow period for a recycled pulsar and minimum companion mass of $\sim$0.5 $M_\odot$, this system is mostly indicative of a carbon oxygen white dwarf (CO WD) companion (Tauris, Langer & Kramer 2011, 2012).

8.2 Mildly recycled pulsars

Here we highlight some MMGPS pulsars with spin periods between 20 and 100 ms. Pulsars with spin periods in this range could be young pulsars born from a recent supernova event (e.g. Crab Pulsar). They could also be binary systems whose recycling process via mass transfer from a companion was interrupted early. If the companion underwent a supernova and the binary survives, it could form a DNSs with a significant eccentricity due to the sudden mass loss and imparted kick (e.g. Tauris et al. 2017). Alternatively, a similar spinning mildly recycled system could also have a high-mass WD companion with a mild eccentricity ($e < 0.01$, see e.g. PSR J2222−0137; Guo et al. 2021). If the binary is disrupted, it leads to two isolated NSs.

8.2.1 PSR J1208−5936

PSR J1208−5936 was detected at a spin period of 28.7 ms at a high DM of 344 pc cm^{-3} with an S/N of 15 in the FFT and 19 in the diagnostic folds. It is a mildly recycled pulsar in an eccentric ($e = 0.348$) 15-h orbit around a companion with a minimum mass of $\sim$1.1 $M_\odot$. This suggests a DNS nature of the system, which has been confirmed through the measurement of post-Keplerian parameters with pulsar timing. Because of its compactness, eccentricity and large mass, the system is predicted to merge within the Hubble time due to gravitational wave radiation. A thorough study and description of this system will be presented in Bernardich et al. (in preparation).

8.2.2 PSR J1155−6529

PSR J1155−6529 was discovered at S/N 18 with $P = 78.9$ ms and a low DM of 33 pc cm^{-3}. Changing barycentric periods from early observing epochs quickly revealed the pulsar to be in a binary system. The orbital solution gives $P_b = 3.67$ d, $x = 15.34$ lt-s, and $e = 0.26$ implying a minimum companion mass of 1.27 $M_\odot$. After monitoring this pulsar for nearly a year, a phase-connected solution was obtained. The spin period derivative ($\dot{P}$) was estimated to be $\sim 3.5 \times 10^{-19}$ s s^{-1} indicating that the pulsar is most likely mildly

[32] All discoveries are catalogued at http://www.trapum.org/discoveries/

Table 3. Summary of the 78 newly discovered pulsars from the MMGPS-L survey. The parameters are the spin period (P), dispersion measure (DM), and the signal-to-noise ratio (S/N) as observed in the discovery epoch. The current best known position in right ascension (RA) and declination (Dec.) is also given for each discovered pulsar. The values listed here are not final. Coherent timing solutions for each of the pulsars will be published elsewhere.

PSR	P (s)	DM (pc cm^{-3})	S/N	RA (hh:mm:ss)	Dec. (°:′:″)
J0853−4648	0.4731561(47)	304(1)	10.98	08:53:21.33	− 46:48:56.10
J0916−5243	1.3104443(32)	162.60(37)	36.98	09:16:09.15	− 52:43:44.40
J0917−4413	0.052905412(70)	123.80(16)	9.65	09:17:52.4090[a]	− 44:13:20.4000[a]
J0922−4534	0.00441655939(42)	113.933(14)	28.89	09:22:16.55	− 45:34:41.00
J0927−5242[c]	0.3279513(24)	296(1)	15.12	09:27:14.86	− 52:42:18.60
J0933−4604	3.669913(48)	123(2)	19.26	09:33:52.13	− 46:04:47.20
J0936−4750	0.522581(10)	113(3)	14.37	09:36:41.58	− 47:50:30.60
J0948−5549	0.1660954(18)	178(1)	8.52	09:48:12.28	− 55:49:16.90
J0954−5754[b]	0.0048352732(19)	307.349(55)	13.65	09:54:53.512[a]	− 57:54:48.6999[a]
J1001−5603	0.3795330(27)	235.30(99)	13.89	10:01:04.97	− 56:03:10.00
J1015−5359[b]	0.020800497(23)	30.80(16)	9.70	10:15:57.7514[a]	− 53:59:11.9999[a]
J1020−5510	0.00394277797(25)	134.8000(89)	32.07	10:20:31.93	− 55:10:07.80
J1020−6158	0.28287863(52)	363.00(26)	17.03	10:20:12.25	− 61:58:51.70
J1030−6008[b]	0.0273244607(83)	370.800(38)	22.25	10:30:26.1646[a]	− 60:08:37.3999[a]
J1034−5817	0.791478(37)	579(6)	10.77	10:34:28.66	− 58:17:57.50
J1034−5934[b]	0.034471431(78)	603.80(32)	12.33	10:34:36.555[a]	− 59:34:21.8497[a]
J1039−6108	0.2715526(13)	488.20(69)	14.33	10:39:36.72	− 61:08:46.20
J1039−6208	1.2465626(89)	281.80(99)	26.14	10:39:08.90	− 62:08:18.10
J1051−6214	1.146050(33)	246(4)	13.44	10:51:36.56	− 62:14:56.50
J1108−6329[b]	0.0042775833(16)	233.200(52)	15.38	11:08:51.3223[a]	− 63:29:24.2993[a]
J1134−6207	0.688961(10)	662(2)	16.96	11:34:03.67	− 62:07:08.20
J1138−6154	0.6243723(48)	456(1)	14.97	11:38:20.57	− 61:54:47.20
J1148−6546	1.4967432(22)	121.50(21)	37.53	11:48:24.58	− 65:46:25.90
J1155−6529[b]	0.078869839(73)	33.00(14)	18.16	11:55:13.26[a]	− 65:29:18.5[a]
J1208−5936[b]	0.02870611(11)	344.20(50)	19.09	12:08:27.0301[a]	− 59:36:20.3812[a]
J1212−5838[c]	0.07380210(38)	145.86(74)	33.11	12:12:47.1913[a]	− 58:38:34.8999[a]
J1231−5929	0.4098337(18)	356.20(62)	17.08	12:31:42.56	− 59:29:12.5
J1232−5843	0.28531841(94)	207.50(48)	15.52	12:32:06.26	− 58:43:31.70
J1244−6437	0.21290473(77)	321.58(54)	16.41	12:44:11.99	− 64:37:59.00
J1306−6043[b]	0.0056711609(41)	67.05(10)	18.77	13:06:20.2027[a]	− 60:43:47.4999[a]
J1316−6147	1.93258(20)	625(13)	13.95	13:16:33.68	− 61:47:23.00
J1328−6605	0.7343669(21)	329.30(39)	29.61	13:28:46.64	− 66:05:48.70
J1338−6425[b]	0.0040877977(13)	85.920(46)	15.66	13:38:24.1796[a]	− 64:25:13.6996[a]
J1352−6141	0.00473833705(63)	76.300(19)	13.03	13:52:01.48	− 61:41:25.8
J1353−6341[c]	2.07616(72)	439(49)	13.95	13:53:31.0256[a]	− 63:41:31.0991[a]
J1359−6242	0.899747(13)	784(2)	11.27	13:59:30.25	− 62:42:22.5
J1408−6009	0.5676345(55)	546(1)	16.75	14:08:14.2	− 60:09:58.5
J1409−6011	0.3005806(13)	448.60(60)	12.94	14:09:48.32	− 60:11:23.5
J1413−5936[b]	0.021676252(36)	366.00(23)	11.82	14:13:50.6266[a]	− 59:36:08.1995[a]
J1426−6136	0.28370007(56)	722(3)	15.25	14:26:11.67	− 61:36:47.30
J1436−6405[c]	0.0093329712(32)	148.200(43)	13.49	14:36:37.2304[a]	− 64:06:28.4999[a]
J1449−6339[c]	0.02946618(13)	75.38(51)	19.00	14:49:54.3805[a]	− 63:39:24.8[a]
J1452−5549[c]	0.07525272(46)	184.4(90)	27.76	14:52:07.4596[a]	− 55:49:16.8999[a]
J1454−5416	0.39645935(56)	141.74(19)	31.87	14:54:29.76	− 54:16:50.00
J1500−6054	0.2136614(11)	419.23(73)	10.62	15:00:43.16	− 60:54:21.40
J1510−5254[b]	0.00477903279(89)	31.935(22)	13.62	15:10:26.6852[a]	− 52:54:39.2999[a]
J1512−6029	0.2295951(17)	337(1)	11.28	15:12:27.15	− 60:29:55.20
J1520−5402	0.2706992(14)	33.70(63)	15.60	15:20:52.19	− 54:02:05.40
J1526−5652	0.8489129(27)	430.00(44)	20.21	15:26:30.07	− 56:52:4.90
J1529−5102	1.2684544(75)	193.80(87)	22.80	15:29:25.56	− 51:02:58.00
J1529−5609[b]	0.036032315(24)	127.800(84)	22.18	15:29:58.4120[a]	− 56:09:50.2999[a]
J1530−5724	0.5680300(13)	253.60(34)	17.30	15:30:25.08	− 57:24:37.1
J1536−6142	0.369501(14)	292(5)	23.01	15:36:57.7740[a]	− 61:42:11.5996[a]
J1536−6149[b]	0.0068751628(29)	245.000(59)	38.70	15:36:58.5299[a]	− 61:49:59.7997[a]
J1540−5821	3.474718(72)	427(3)	24.21	15:40:10.60	− 58:21:55.50
J1543−5439[b]	0.00431230524(20)	102.1635(62)	50.23	15:43:29.2261[a]	− 54:39:22.9[a]
J1547−5056	0.4527822(33)	107(1)	16.28	15:47:04.79	− 50:56:19.00
J1554−4854	0.4647786(11)	255.60(33)	29.22	15:54:42.68	− 48:54:01.5
J1554−5906[b]	0.0087021481(23)	130.132(39)	15.14	15:54:44.2288[a]	− 59:06:41.6997[a]
J1604−4832	0.007718008(16)	207.80(28)	8.52	16:04:47.2307[a]	− 48:33:06.0995[a]

Table 3 – *continued*

PSR	*P* (s)	DM (pc cm^{-3})	S/N	RA (hh:mm:ss)	Dec. (°: ′: ″)
J1610−4938	0.2274187(12)	365.00(77)	12.25	16:10:59.14	−49:38:09.30
J1614−4608	0.888793(13)	318(2)	18.97	16:14:42.97	−46:08:36.90
J1615−5609[b]	0.00335913002(30)	72.025(12)	25.47	16:15:49.6201[a]	−56:09:32.8[a]
J1623−4608	0.8663065(40)	109.99(63)	21.40	16:23:27.77	−46:08:01.60
J1623−4931	0.4923472(55)	727(1)	20.51	16:23:32.57	−49:31:08.00
J1633−4859	2.51478(15)	1020(9)	22.21	16:33:04.56	−48:59:03.70
J1636−4217	0.5550858(48)	345(1)	8.49	16:36:21.22	−42:17:30.7
J1645−4836	1.660076(42)	687(4)	23.81	16:45:51	−48:36:41
J1649−3752	0.5872420(19)	222.90(50)	24.75	16:49:11.35	−37:52:15.90
J1649−4230	0.676409(33)	374(6)	19.53	16:49:46.64	−42:30:21.30
J1650−5025[c]	0.059675730(28)	213.500(66)	18.73	16:50:00.1835[a]	−50:26:03.0000[a]
J1652−5154	0.5996810(14)	265.81(34)	27.16	16:52:32.78	−51:54:10.60
J1702−4145	0.345805(15)	945(6)	16.22	17:02:57.48	−41:45:23.90
J1704−3549	2.270547(13)	291.57(88)	26.81	17:04:26.43	−35:49:27.80
J1706−4020	0.1806319(26)	598(2)	10.15	17:06:05.40	−40:20:07.70
J1708−4843[b]	0.0166572656(50)	28.700(40)	17.31	17:08:33.9626[a]	−48:43:31.8000[a]
J1716−3811	0.82912(13)	1219(21)	11.60	17:16:29.62	−38:11:07.8
J1806−2125	0.1720044(41)	555(3)	16.40	18:06:18.2400[a]	−21:25:01.0000[a]

[a]The positions of these pulsars were further constrained based on the multibeam localization as described in Section 6.1.4. The positions of other pulsars are given by the coordinates of the highest S/N beam detection in the discovery epoch.
[b]Binary pulsar.
[c]Isolated pulsar.

recycled. A detailed description of this pulsar will be presented in an upcoming publication (Berezina et al., in preparation).

8.3 Canonical pulsars

The major fraction of discoveries from MMGPS-L are pulsars with spin periods in excess of 100 ms (51 out of 78). Some of the discoveries are briefly discussed below.

8.3.1 PSR J1353−6341

PSR J1353−6341 was the first non-recycled pulsar discovery (second overall) discovered with S/N 14 with a spin period of 2.0764 s at a DM of 435 pc cm^{-3}. The barycentric spin period between the discovery and confirmation observations is consistent with the pulsar being isolated. The discovery observation however revealed a possibility of nulling or intermittency. Follow-up observations revealed the pulsar to null on a time-scale of 1–3 min thus switching between the off and on states multiple times in an observation. The pulsar is currently being followed up with the Parkes telescope.

8.3.2 PSR J0933−4604

PSR J0933−4604 is the slowest rotating pulsar discovered in the MMGPS-L survey so far. It was discovered with S/N 19 with a spin period of 3.67 s at a DM of 123 pc cm^{-3}. Similar to J1353−6141, the discovery observation revealed a possibility of nulling or intermittency. This discovery demonstrates that MMGPS-L is capable of finding pulsars with spin periods of the order of several seconds even though short observations and use of FFT-based search techniques (see e.g. Morello et al. 2020) are less sensitive to slow spinning pulsars.

Besides time-domain techniques, we are also investigating continuum images in fields corresponding to the pointings where the new pulsar discoveries were made. Identification of point sources in these fields that match with the localized positions of the pulsars can better characterize the flux and spectral index of these sources.

9 EARLY RESULTS FROM IMAGING AND SPECTRAL LINE STUDIES

In this section, we use joint SARAO–MPIfR commissioning observations at S-band of the Sagittarius B2 (Sgr B2) region to demonstrate the continuum and spectral line imaging capabilities of MMGPS. Sgr B2 is located close to the Galactic Centre at a distance of ∼8.15 kpc (Reid et al. 2019) and is one of the most massive star-forming regions in the Milky Way. Furthermore, Sgr B2 has been the focus of numerous spectroscopic surveys (e.g. Belloche et al. 2013, 2016, 2019; Corby et al. 2015) owing to its prominence in the central molecular zone (CMZ; e.g. Henshaw et al. 2022, and references therein) and hence forms an ideal test bed for commissioning.

We observed the Sgr B2 region on 2021 September 16 using 50 MeerKAT dishes fitted with the S-band receiver, with the telescopes pointed at 17:47:20.5, −28:23:06.0 (J2000). The visibility data were recorded using the S4 filter covering the frequency range 2626–3500 MHz. This frequency coverage was divided into 32k channels resulting in a channel frequency resolution of 26.703 kHz. The 10-min scan on Sgr B2 was book-ended by two scans on the phase calibrator J1733−1304. We also observed J1939−6342 and 3C 286 as flux density, bandpass, and polarization angle calibrators.

The visibility data were calibrated and imaged using the pipeline described in Section 6.2. Fig. 6 shows the wide-band Stokes *I* multifrequency synthesis (MFS) image, whose synthesized beam has a FWHM of 3.8 × 2.4 arcsec^2. The rms noise in the Stokes *I* and *V* MFS images are 75 and 27 μJy PSF^{-1}, respectively. For a SEFD of ∼450 Jy, the theoretical point source sensitivity expected for our observation assuming a natural visibility weighting scheme is ∼10 μJy PSF^{-1}.

With the narrow-band correlator mode not available at the time of the observations, we used the same wide-band 32k observations to

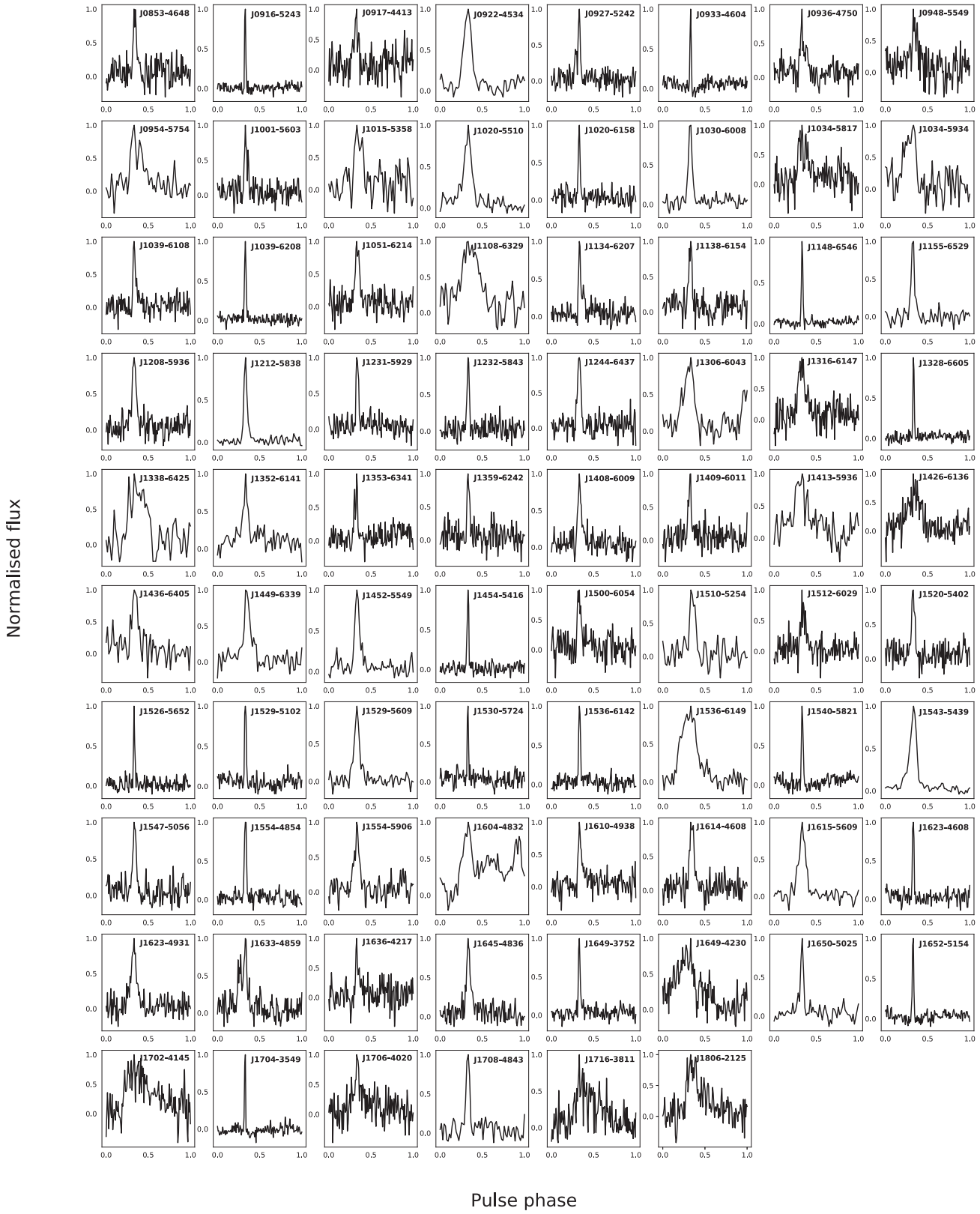

Figure 5. Pulse profiles from the respective discovery epochs of the 78 new pulsars of the MMGPS-L survey.

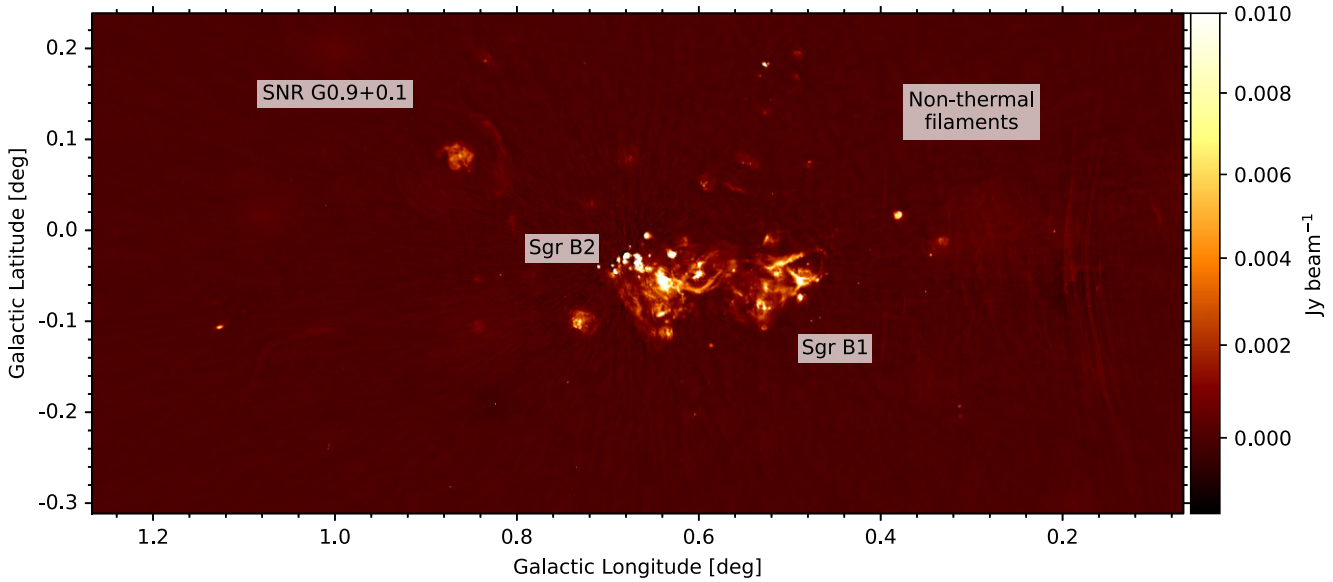

Figure 6. Broad-band total intensity image of the Sgr B2 region observed using the S4 (2626–3500 MHz) filter on MeerKAT. The FWHM of the synthesized beam is 3.8 × 2.4 arcsec^2 and the rms noise in the image is 75 μJy PSF^{-1}.

verify spectral line capabilities of MeerKAT towards the CH HFS transitions at 3.3 GHz. As reference spectra we used observations of Sgr B2 by Jacob et al. (2021) with the JVLA. The channel width of 27.703 kHz in the MeerKAT 32k wide-band provides a spectral resolution of ∼2.5 km s^{-1} at 3.3 GHz. While this is too coarse to resolve typical line-of sight features with narrow line widths, it is sufficient to resolve lines associated with Sgr B2 itself. In addition to simultaneously covering all HFS splitting transitions of CH (see Table 1), the wide bandwidth encompasses 13 hydrogen radio recombination lines (RRLs), of which 11 are within usable ranges of the band.

The spectral lines were calibrated separately from the continuum as described in Section 6.3. For each line, we selected channels within ±300 km s^{-1} of the line rest frequency for further processing. We did not apply Hanning smoothing to the data, and automatic flagging was applied only to calibration scans. The continuum was subtracted from the data in the *uv*-plane. The data were imaged and deconvolved with `tclean` in CASA.[33] To compare MeerKAT with VLA observations, the MeerKAT data were tapered and smoothed to match an angular resolution of 23 arcsec. The CH transitions were imaged at a native channel resolution of ∼2.5 km s^{-1}. In order to increase the sensitivity on the radio recombination line emission, we chose a subset of the radio recombination lines (H129α–H124α) and imaged them at 5 km s^{-1} spectral resolution. We stacked the maps at each velocity after smoothing all lines to an angular resolution of 23 arcsec.

Fig. 7 shows a close-up of the Sgr B2 star-forming complex, with multiple subcomponents of the region, such as Sgr B2 (M) and Sgr B2 (N). The 10 cm continuum emission from MeerKAT overlaid with the ALMA 3 mm continuum emission (Ginsburg et al. 2018), which traces both free–free and dust emission, shows several embedded H II regions (e.g. Meng et al. 2022). The CH 0^-–1^+ transition is seen in emission towards the source velocities of Sgr B2 (N) and Sgr B2 (M) near 64 km s^{-1}, with a mixture of emission and absorption seen in the weaker CH 1^-–1^+ and CH 1^-–0^+ transitions. For all three lines, weak emission originates from clouds along the line of sight. We detect radio recombination line emission towards both transitions (see also e.g. Meng et al. 2019), which provides information on the physical and kinematic properties of the numerous (ultra)compact H II regions in Sgr B2.

This image demonstrates the imaging capabilities of the telescope for a source, providing high angular resolution and sensitivity, for a source with very complex emission structure. Furthermore, on the right-hand panels of Fig. 7, we compare the MeerKAT commissioning observations to JVLA observations from Jacob et al. (2021) at a common resolution of 23 arcsec. Overall, we find excellent agreement between the MeerKAT and JVLA observations, which gives confidence for official science operations of future spectral line observations. We note that the original JVLA data reveal narrow CH features that are not resolved at the spectral resolution of the wide S-band 32k channel mode. Therefore, future observations of the ground state radio lines of CH will be conducted in a separate narrow-band mode at L-band with a channel width of 1.633 kHz, which corresponds to a spectral resolution of ∼0.3 km s^{-1} at the H I and OH transitions at L-band.

10 DISCUSSION AND FUTURE PROSPECTIVE

The MMGPS commensal survey has demonstrated a unique approach to large-scale surveys in terms of key scientific drivers and the development of the corresponding instrumentation and processing infrastructure.

In the time domain, we have predominantly focused on searches for radio pulsars with a priority of finding compact binary systems and have made significant inroads on this front. Of the 78 discoveries so far, 17 are confirmed to be in binaries with PSR J1015−5359 being the most compact (P_b = 7.9 h) of them all. The ratio of binaries to total discoveries is almost 1:5 that is more than twofold higher than the average (1:13)[34] ratio based on known pulsars in

[33] CASA version 5.7.2 was used for imaging the spectral line data presented in this work.

[34] This is based on the pulsars listed in the ATNF catalogue (Manchester et al. 2005) after excluding pulsars in globular clusters.

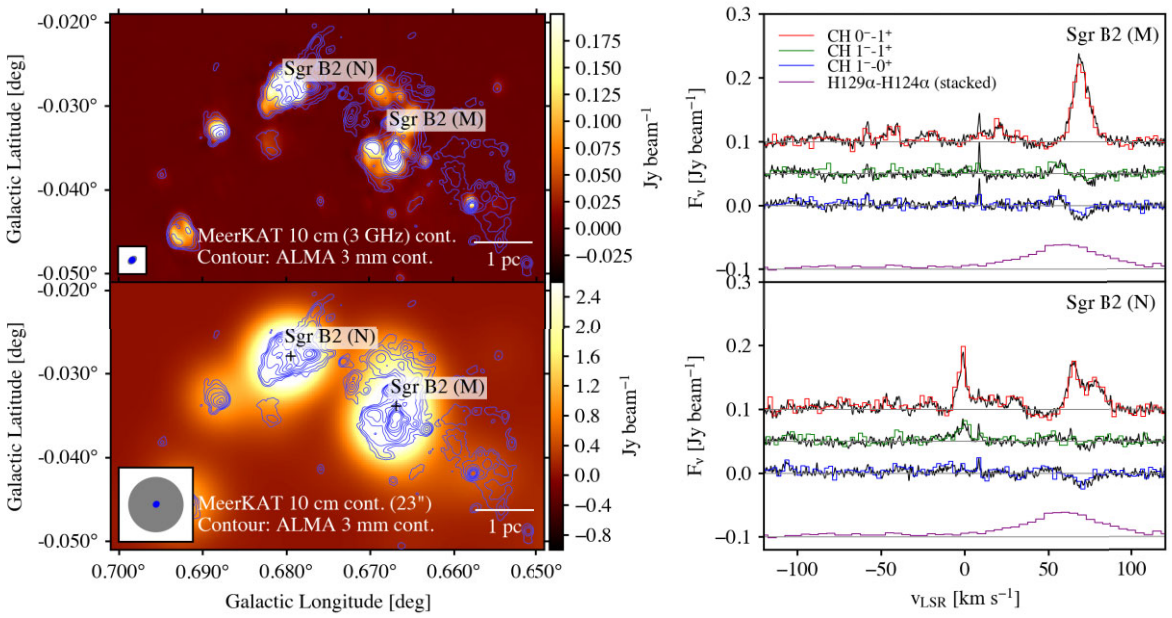

Figure 7. Top left: zoom-in on the Sgr B2 star-forming complex, image as in Fig. 6. Contours show ALMA 3 mm continuum emission from Ginsburg et al. (2018) at 2.3 × 2.0 arcsec^2 resolution in levels of 6, 11, 20, 50, 100, 200, 300, 500, and 1000 mJy beam^{-1}. The restoring beams of the MeerKAT and ALMA observations are indicated by grey and blue ellipses on the bottom left, respectively. The scale bar on the bottom right indicates the angular size corresponding to a physical size of 1 pc at a distance of 8.15 pc (Reid et al. 2019). Bottom left: MMGPS 3 GHz continuum image smoothed to 23 arcsec resolution, illustrating the spatial resolution of the spectral line maps from which the spectra on the right are extracted. Contours and labels as above. The positions of the spectra are indicated by black crosses. Right-hand panels: CH hyperfine splitting transitions at 3.3 GHz observed with the S4 32k wide-band mode towards Sgr B2 (M) and (N) with a spectral resolution of ∼2.5 km s^{-1} and after smoothing all data to 23 arcsec resolution. For comparison, we show a subset of the observed hydrogen radio recombination lines (H129α–H124α) tracing ionized gas, which were stacked in velocity to increase sensitivity at 5 km s^{-1}. As part of commissioning, the CH observations were found to be consistent with previous JVLA observations (Jacob et al. 2021), which are plotted for comparison in black.

the Galactic field. The large fraction of binaries have primarily been a consequence of short observations coupled with acceleration searches thus improving the sensitivity to a larger volume of the binary pulsar parameter space. Comparing the binary discoveries with the Galactic field population reveals that the orbital properties are consistent with what is typically found in the Galaxy. This is demonstrated in Fig. 8 where the orbital period is plotted against the projected semimajor axis for all Galactic field binaries and the MMGPS-L discoveries.

The spin-period distribution of the discoveries when compared to the known pulsar population in the same field as MMGPS-L reveals a significantly different distribution (as evidenced by the Kolmogorov–Smirnov test giving a p-value = 0.007). Interestingly, a significant fraction of discoveries (12 out of 74) are in the mildly recycled or young pulsar period regime ($20 < P < 100$ ms) and has increased the known pulsar population in this parameter space by more than 7.5 per cent. There are also a class of potential MSPs with CO WD companions (J1015−5359 and J1338−6425) whose nature if confirmed could put additional constraints for the evolution process of these systems in the Galactic field (e.g. Tauris et al. 2011, 2012). The two potential DNSs (J1208−5936 and J1155−6529) may be interesting for testing gravity in the strong field regime by measuring post-Keplerian parameters in the coming years (e.g. Kramer et al. 2021). PSR J1208−5936 is expected to merge within Hubble time and would hence also add further constraints on the DNS merger rate in the Galaxy (e.g. Pol, McLaughlin & Lorimer 2019; Grunthal, Kramer & Desvignes 2021; Bernadich et al., in preparation). Moreover, PSR J1306−6043 offers the scope for multiwavelength follow-up studies in radio and gamma-rays similar to previous such analyses (e.g. Johnson et al. 2014).

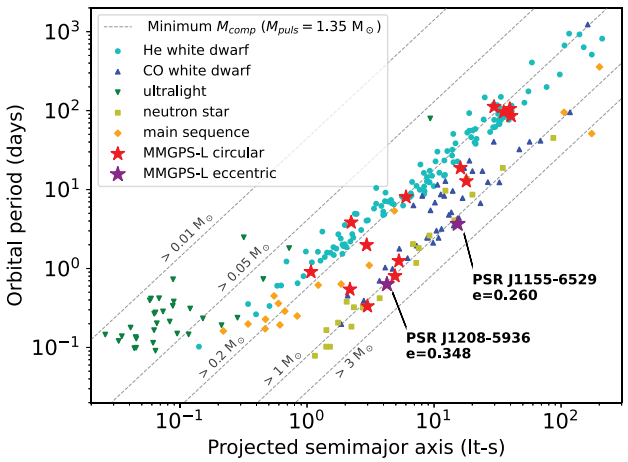

Figure 8. Comparison of the binary pulsars discovered by MMGPS-L with the known binaries in the Galactic field excluding pulsars in globular clusters (data are taken from the ATNF catalogue; Manchester et al. 2005). Binary pulsars whose companion mass nature is known are also provided for distinction. Lines of constant minimum companion mass ($M_{\rm comp}$) are represented as grey dashed lines. $M_{\rm comp}$ is calculated assuming the pulsar mass to be 1.35 M$_\odot$. The eccentric systems found in the MMGPS-L so far are marked separately.

With the science operations at S-band commencing soon, the aim and expectation from the pulsar searching aspect is not necessarily a high number of exciting discoveries but rather a few select discoveries whose properties are outliers in the standard pulsar parameter space.

Regarding MSPs, MMGPS-L has already pushed the record for the highest DM in its sky region by ∼40 pc cm^{-3} (PSR J1208−5936 with a DM = 344.2 pc cm^{-3} compared to PSR J1325−6256 with a DM = 303.3 pc cm^{-3}). Moreover, the non-recycled pulsar discoveries with MMGPS-L average a higher DM than MSP discoveries. This is no surprise given that MSPs are more prone to dispersive smearing and scattering. Thus the expectation at S-band is pulsar discoveries (recycled and non-recycled) at high DMs and flatter spectral indices than average. While the integration time is a factor of 2 higher than at L-band, MMGPS-S will still be sensitive to compact binary systems with orbital periods above 3 h. Keeping this in mind, it is worth pushing the boundaries of the current search parameter space used for MMGPS-L. However, unlike previous Galactic plane surveys where data have been stored offline and undergone multiple iterations of searches with new techniques (e.g. Eatough et al. 2013a; Cameron et al. 2020), the raw data from MMGPS need to be deleted. Thus any additional search to be conducted on the data should make sure that the fraction of processing time compared to the already established search space is minimal. One possibility is to downsample the data and expand the acceleration range for the data without increasing the processing speed significantly. This could be an advantage when probing for DNSs or the elusive pulsar–black hole systems where the binary evolution prevents the pulsar from spinning up to very rapid spin frequencies. The detection of a binary NS merger (Abbott et al. 2017) and more recently multiple NS and black hole mergers (Abbott et al. 2021) motivate such a search to be conducted.

Complementary and contrary to the S-band, the survey at UHF is expected to yield low DM discoveries (owing to higher dispersion at low frequencies) and a significant number of binary pulsars (owing to the similar dwell time to MMGPS-L). Moreover, the last comparable southern survey for pulsars at a similar frequency was the Parkes 70 cm survey (PKS70; Manchester et al. 1996). The MMGPS-UHF survey is estimated to be 20 times more sensitive than PKS70, thus offering significant prospects for a large number of discoveries. Estimating the number of expected discoveries for each of the subsurveys operating at different observing frequencies is non-trivial. As a first-order approximation, we used the parameters of each subsurvey as an input to PsrPopPy (Bates et al. 2014), which is a software package for pulsar population synthesis. We then applied a constant correction factor to account for the inconsistent coverage across the survey beam (based on the discussion in Section 7.3) and would thus decrease the overall yield. Adding the numbers from each of the three subsurveys, our expected yield is roughly 500 canonical pulsars and 45 MSPs. However, it is important to note that these numbers are not robust. Every pointing has a different tiling pattern of coherent beams and would thus yield differences in coverage and sensitivity. A detailed analysis predicting the survey pulsar yield after accounting for the coverage constraints will be presented in a future publication.

Traditionally, large area imaging surveys of the southern Galactic plane like the S-band Polarization All-Sky Survey (S-PASS; Carretti et al. 2019) have been carried out with single-dish telescopes resulting in spatial resolutions of the order of a few arcminutes. With the advent of SKA precursor instruments in the Southern hemisphere, it is now possible to map the radio synchrotron emission from the southern Galactic plane with subarcminute resolution (e.g. see Umana et al. 2021). As has been demonstrated in Section 9, the imaging component of MMGPS will deliver radio maps with sensitivities of the order of a few tens of micro-Jansky (μJy) with a spatial resolution of a few arcseconds, thus opening a new window to parts of the southern Galactic plane. Moreover, the sensitivity of the S-band component will be unsurpassed even in the initial decades of the SKA era as the SKA MID Band 3 and 4 receivers covering the 1.65–3.05 and 2.80–5.18 GHz frequency ranges, respectively, are not part of the current design baseline (e.g. see Braun et al. 2019).

The commensal mode of operation between different domains also presents the opportunity of one science case giving and receiving feedback from the other that can in turn help further refine the scientific goals. Given that pulsars show negative spectral indices (e.g. Jankowski et al. 2018), any newly catalogued steep spectrum sources from imaging could be followed up in the time domain. This can be done by placing a tied array beam on the best reference position and searching for radio pulsations using the pulsar and transient search pipelines. Several such successful targeted pulsar searches based on spectral information have been conducted in the past (e.g. Backer et al. 1982; Navarro et al. 1995; Bhakta et al. 2017). Imaging can also reveal SNRs associated with newly discovered pulsars. Finally, accurate RM measurements of the discovered pulsars in the long term will provide an indirect imprint of the Galactic magnetic field along the line of sight.

Over the past decade, spectral line observations of light hydrides (like CH and OH) at sub-mm and far-infrared wavelengths have revealed their use as powerful tracers for different phases of the ISM (see Gerin, Neufeld & Goicoechea 2016, for more information). Furthermore, lying at an early stage of interstellar chemistry observations of light hydrides is imperative for extending our understanding of the growth of chemical complexity in star-forming regions. However, limited access to the sub-mm and far-infrared skies (with the end of the *Herschel* and SOFIA missions) restrict observations of the high-lying rotational transitions of light hydrides renewing interests in their ground state radio lines.

As discussed in the previous sections, observations of all three of the ground state HFS splitting lines of CH, H I at 21 cm, and three of the four ground state HFS splitting transitions of OH are planned in different tunings for ∼20 positions along the Galactic plane, primarily to complement far-infrared observations taken as a part of the SOFIA Legacy program HyGAL (as discussed in Section 2.3). The ground state lines of OH at 18 cm (Rugel et al. 2018) like that of CH are plagued by anomalous excitation effects that in a manner similar to that described for CH can be resolved when analysed jointly with its far-infrared lines at 2.5 THz observed under the HyGAL program thereby extending its use as a powerful diagnostic tool at radio wavelengths. Furthermore, while CH and OH probe diffuse and translucent molecular cloud conditions, molecular ions like ArH^+, H_2O^+, and OH^+ observed under HyGAL trace diffuse atomic gas (Schilke et al. 2014; Indriolo et al. 2015; Neufeld & Wolfire 2017; Jacob et al. 2020). The molecular fraction or the ratio of molecular gas to the total gas column in a given volume is an important quantity used to distinguish between the different ISM phases discussed above making observations of the H I 21 cm line essential.

11 CONCLUSIONS

We have presented the various aspects of the observing, data recording, and processing set-up for the MMGPS. This 3000-h commensal survey uses the telescope time for multiple science cases covering time, imaging, and spectral line domains. The survey consists of four subsurveys consisting of a shallow L-band (856–1712 MHz) survey, a deep S-band survey (2–3 GHz) primarily restricted to the plane ($b < 1.5°$), a survey focused on the Galactic Centre (3 GHz), and a dedicated spectroscopy survey targeting CH, H I, and OH molecules. We have completed the L-band survey with the S-band receivers soon to begin science operations. We have discovered 78 new

pulsars so far including a mixture of MSPs, mildly recycled pulsars, and canonical pulsars. Notable mentions are PSR J1208−5936 and PSR J1155−6529 that are potential DNSs. The high spatial resolution and broad frequency coverage of the imaging data products from MMGPS open a new window into parts of the southern Galactic plane with its unparalleled sensitivity. In the upcoming series of papers, we aim to publish the total intensity, spectral index, and polarization data products derived from our L- and S-band observing campaign. Furthermore, spectral line commissioning observations at S-band of the CH hyperfine-structure splitting transitions at 3.3 GHz towards previously studied star-forming complexes like Sgr B2(M) explore the capabilities of the MeerKAT system for future spectroscopic studies of important tracers of the diffuse and translucent skies. These initial results have demonstrated the enhanced scientific and technological capability of MeerKAT. It has also laid a foundation for thorough planning of future large-scale surveys particularly with the SKA.

ACKNOWLEDGEMENTS

The MeerKAT telescope is operated by the South African Radio Astronomy Observatory, which is a facility of the National Research Foundation, an agency of the Department of Science and Innovation. SARAO acknowledges the ongoing advice and calibration of GPS systems by the National Metrology Institute of South Africa (NMISA) and the time space reference systems department of the Paris Observatory. This work has made use of the 'MPIfR S-band receiver system' designed, constructed, and maintained by funding of the MPI für Radioastronomy and the Max Planck Society. The authors acknowledge colleagues, engineers, and scientists at SARAO for their tremendous help in installing and commissioning the S-band system. We are also in particular grateful to all MPIfR engineers and technicians responsible for developing, building, and installing the S-band system. Observations used the FBFUSE and APSUSE computing clusters for data acquisition, storage, and analysis. These clusters were funded and installed by the Max-Planck-Institut für Radioastronomie (MPIfR) and the Max-Planck-Gesellschaft. The authors acknowledge continuing valuable support from the Max Planck Society. We thank the referee for valuable comments which helped improve the clarity of the paper. MRR is a Jansky Fellow of the National Radio Astronomy Observatory. AMJ acknowledges support from USRA through a grant for SOFIA Program 08_0038. MBe acknowledges support from the Bundesministerium für Bildung und Forschung (BMBF) D-MeerKAT award 05A17VH3 (Verbundprojekt D-MeerKAT). MBu acknowledges support through the research grant 'iPeska' (PI: Andrea Possenti) funded under the INAF national call Prin-SKA/CTA approved with the Presidential Decree 70/2016. MMN acknowledges support in part by the National Science Foundation under Grant No. NSF PHY-1748958.

DATA AVAILABILITY

The data at L-band underlying this paper will be shared on reasonable request to the MMGPS Collaboration. The S-band commissioning data used for this paper will be shared on reasonable request to collaborators from MPIfR and SARAO.

REFERENCES

Abbate F., Possenti A., Tiburzi C., Barr E., van Straten W., Ridolfi A., Freire P., 2020, Nat. Astron., 4, 704
Abbott B. P. et al., 2017, Phys. Rev. Lett., 119, 161101
Abbott R. et al., 2021, ApJ, 915, L5
Agarwal D., Aggarwal K., Burke-Spolaor S., Lorimer D. R., Garver-Daniels N., 2020, MNRAS, 497, 1661
Anderson C. S., Gaensler B. M., Feain I. J., Franzen T. M. O., 2015, ApJ, 815, 49
Anderson L. D. et al., 2017, A&A, 605, A58
Antoniadis J., 2014, ApJ, 797, L24
Antoniadis J. et al., 2013, Science, 340, 448
Antoniadis J. et al., 2022, MNRAS, 510, 4873
Arras P., Reinecke M., Westermann R., Enßlin T. A., 2021, A&A, 646, A58
Ashok A. et al., 2021, ApJ, 923, 85
Backer D. C., Kulkarni S. R., Heiles C., Davis M. M., Goss W. M., 1982, Nature, 300, 615
Bailes M. et al., 2020, Publ. Astron. Soc. Aust., 37, e028
Barr E. D., 2018, in Weltevrede P., Perera B. B. P., Preston L. L., Sanidas S., eds, Proc. IAU Symp. Vol. 337, Pulsar Astrophysics the Next Fifty Years. Cambridge Univ. Press, Cambridge, p. 175
Barr E., 2020, Astrophysics Source Code Library, record ascl:2001.014
Barr E. D. et al., 2013, MNRAS, 435, 2234
Barsdell B. R., Bailes M., Barnes D. G., Fluke C. J., 2012, MNRAS, 422, 379
Bates S. D., Lorimer D. R., Rane A., Swiggum J., 2014, MNRAS, 439, 2893
Beck R., Brandenburg A., Moss D., Shukurov A., Sokoloff D., 1996, ARA&A, 34, 155
Becker R. H., White R. L., Helfand D. J., Zoonematkermani S., 1994, ApJS, 91, 347
Belloche A., Müller H. S. P., Menten K. M., Schilke P., Comito C., 2013, A&A, 559, A47
Belloche A., Müller H. S. P., Garrod R. T., Menten K. M., 2016, A&A, 587, A91
Belloche A., Garrod R. T., Müller H. S. P., Menten K. M., Medvedev I., Thomas J., Kisiel Z., 2019, A&A, 628, A10
Beltrán M. T. et al., 2013, A&A, 552, A123
Benjamin R. A. et al., 2003, PASP, 115, 953
Beuther H. et al., 2016, A&A, 595, A32
Bezuidenhout M. C. et al., 2023, RAS Techniques and Instruments, 2, 114–128
Bhakta D., Deneva J. S., Frail D. A., de Gasperin F., Intema H. T., Jagannathan P., Mooley K. P., 2017, MNRAS, 468, 2526
Bhattacharyya B. et al., 2016, ApJ, 817, 130
Bower G. et al., 2019, BAAS, 51, 438
Braun R., Bonaldi A., Bourke T., Keane E., Wagg J., 2019, preprint (arXiv:1912.12699)
Briggs D., 1995, PhD thesis, New Mexico Institute of Mining and Technology, Socorro, NM
Brown J. C., Haverkorn M., Gaensler B. M., Taylor A. R., Bizunok N. S., McClure-Griffiths N. M., Dickey J. M., Green A. J., 2007, ApJ, 663, 258
Brunthaler A. et al., 2021, A&A, 651, A85
Cameron A. D. et al., 2018, MNRAS, 475, L57
Cameron A. D. et al., 2020, MNRAS, 493, 1063
Camilo F. et al., 2018, ApJ, 856, 180
Carretti E. et al., 2019, MNRAS, 489, 2330
Caswell J. L. et al., 2010, MNRAS, 404, 1029
Chen W., Barr E., Karuppusamy R., Kramer M., Stappers B., 2021, J. Astron. Instrum., 10, 2150013
Corby J. F. et al., 2015, MNRAS, 452, 3969
Cordes J. M. et al., 2006, ApJ, 637, 446
Czech D. et al., 2021, PASP, 133, 064502
Dagdigian P. J., 2018, MNRAS, 475, 5480
Dahal P. K., 2020, J. Astrophys. Astron., 41, 8
Deneva J. S., Cordes J. M., Lazio T. J. W., 2009, ApJ, 702, L177
Desvignes G. et al., 2018, ApJ, 852, L12
Dewdney P. E., Hall P. J., Schilizzi R. T., Lazio T. J. L. W., 2009, Proc. IEEE, 97, 1482
Dickey J. M. et al., 2013, Publ. Astron. Soc. Aust., 30, 3
Dokara R. et al., 2021, A&A, 651, A86
Dokara R. et al., 2022, A&A, 671, A145

Dubner G., Giacani E., 2015, A&AR, 23, 3
Eatough R. P., Kramer M., Lyne A. G., Keith M. J., 2013a, MNRAS, 431, 292
Eatough R. P. et al., 2013b, Nature, 501, 391
Eatough R. P. et al., 2021, MNRAS, 507, 5053
Elia D. et al., 2021, MNRAS, 504, 2742
Faucher-Giguère C.-A., Kaspi V. M., 2006, ApJ, 643, 332
Federman S. R., 1982, ApJ, 257, 125
Fonseca E. et al., 2021, ApJ, 915, L12
Freire P. C. C., Ridolfi A., 2018, MNRAS, 476, 4794
Freire P. C. C., Tauris T. M., 2014, MNRAS, 438, L86
Freire P. C. C. et al., 2011, MNRAS, 412, 2763
Gaensler B. M., Madsen G. J., Chatterjee S., Mao S. A., 2008, Publ. Astron. Soc. Aust., 25, 184
Gaensler B. M., Landecker T. L., Taylor A. R., POSSUM Collaboration, 2010, Am. Astron. Soc. Meeting Abstr., #215, 470.13
Genzel R., Downes D., Pauls T., Wilson T. L., Bieging J., 1979, A&A, 73, 253
Gerin M., Neufeld D. A., Goicoechea J. R., 2016, ARA&A, 54, 181
Ginsburg A. et al., 2018, ApJ, 853, 171
Gravity Collaboration et al., 2019, A&A, 625, L10
Grunthal K., Kramer M., Desvignes G., 2021, MNRAS, 507, 5658
Guo Y. J. et al., 2021, A&A, 654, A16
Han J. L., Manchester R. N., van Straten W., Demorest P., 2018, ApJS, 234, 11
Han J. L. et al., 2021, Res. Astron. Astrophys., 21, 107
Haslam C. G. T., Salter C. J., Stoffel H., Wilson W. E., 1982, A&AS, 47, 1
Haverkorn M., Gaensler B. M., McClure-Griffiths N. M., Dickey J. M., Green A. J., 2006, ApJS, 167, 230
Heald G. et al., 2020, Galaxies, 8, 53
Henshaw J. D., Barnes A. T., Battersby C., Ginsburg A., Sormani M. C., Walker D. L., 2022, preprint (arXiv:2203.11223)
Heywood I. et al., 2022, ApJ, 925, 165
Hoare M. G. et al., 2012, PASP, 124, 939
Indriolo N. et al., 2015, ApJ, 800, 40
Jackson J. M. et al., 2006, ApJS, 163, 145
Jacob A. M., Menten K. M., Wyrowski F., Winkel B., Neufeld D. A., 2020, A&A, 643, A91
Jacob A. M., Menten K. M., Wiesemeyer H., Ortiz-León G. N., 2021, A&A, 650, A133
Jacob A. M. et al., 2022, ApJ, 930, 141
Jankowski F., van Straten W., Keane E. F., Bailes M., Barr E. D., Johnston S., Kerr M., 2018, MNRAS, 473, 4436
Jiang L., Li X.-D., Dey J., Dey M., 2015, ApJ, 807, 41
Johnson T. J. et al., 2014, ApJS, 213, 6
Johnston S., Kramer M., Lorimer D. R., Lyne A. G., McLaughlin M., Klein B., Manchester R. N., 2006, MNRAS, 373, L6
Johnston-Hollitt M. et al., 2015, PoS, AASKA14, 092
Jonas J., MeerKAT Team, 2018, PoS, MeerKAT2016, 001
Keith M. J. et al., 2010, MNRAS, 409, 619
Kocz J., Briggs F. H., Reynolds J., 2010, AJ, 140, 2086
Kocz J., Bailes M., Barnes D., Burke-Spolaor S., Levin L., 2012, MNRAS, 420, 271
Kothes R., Fedotov K., Foster T. J., Uyanıker B., 2006, A&A, 457, 1081
Kouwenhoven M. L. A., Voûte J. L. L., 2001, A&A, 378, 700
Kramer M., Xilouris K. M., Lorimer D. R., Doroshenko O., Jessner A., Wielebinski R., Wolszczan A., Camilo F., 1998, ApJ, 501, 270
Kramer M., Backer D. C., Cordes J. M., Lazio T. J. W., Stappers B. W., Johnston S., 2004, New Astron. Rev., 48, 993
Kramer M. et al., 2006, Science, 314, 97
Kramer M. et al., 2018, PoS, MeerKAT2016, 003
Kramer M. et al., 2021, Phys. Rev. X, 11, 041050
Kurtz S. E., Watson A. M., Hofner P., Otte B., 1999, ApJ, 514, 232
Lang K. R., Wilson R. F., 1978, ApJ, 224, 125
Langer W. D., Velusamy T., Goldsmith P. F., Pineda J. L., Chambers E. T., Sandell G., Risacher C., Jacobs K., 2017, A&A, 607, A59
Li D., Pan Z., 2016, Radio Sci., 51, 1060
Li D. et al., 2018, IEEE Microwave Magazine, 19, 112
Liu K., Eatough R. P., Wex N., Kramer M., 2014, MNRAS, 445, 3115
Liu K. et al., 2021, ApJ, 914, 30
Livingston J. D., McClure-Griffiths N. M., Gaensler B. M., Seta A., Alger M. J., 2021, MNRAS, 502, 3814
Lorimer D. R., 2013, in van Leeuwen J., ed., Proc. IAU Symp. Vol. 291, Neutron Stars and Pulsars: Challenges and Opportunities after 80 years. Cambridge Univ. Press, Cambridge, p. 237
Lorimer D. R., Kramer M., 2004, Handbook of Pulsar Astronomy. Cambridge Univ. Press, Cambridge
Lorimer D. R., Bailes M., McLaughlin M. A., Narkevic D. J., Crawford F., 2007, Science, 318, 777
Lorimer D. R. et al., 2015, MNRAS, 450, 2185
Lyne A. G. et al., 2017, ApJ, 834, 72
Ma Y. K., Mao S. A., Ordog A., Brown J. C., 2020, MNRAS, 497, 3097
McClure-Griffiths N. M., Green A. J., Dickey J. M., Gaensler B. M., Haynes R. F., Wieringa M. H., 2001, ApJ, 551, 394
McClure-Griffiths N. M., Dickey J. M., Gaensler B. M., Green A. J., Haverkorn M., Strasser S., 2005, ApJS, 158, 178
McMullin J. P., Waters B., Schiebel D., Young W., Golap K., 2007, in Shaw R. A., Hill F., Bell D. J., eds, ASP Conf. Ser. Vol. 376, Astronomical Data Analysis Software and Systems XVI. Astron. Soc. Pac., San Francisco, p. 127
Magnani L., Onello J. S., 1993, ApJ, 408, 559
Magnani L., Sandell G., Lada E. A., 1992, A&AS, 93, 509
Malov I. F., 2021, MNRAS, 502, 809
Manchester R. N. et al., 1996, MNRAS, 279, 1235
Manchester R. et al., 2001, MNRAS, 328, 17
Manchester R. N., Hobbs G. B., Teoh A., Hobbs M., 2005, AJ, 129, 1993
Mao S. A. et al., 2014, preprint (arXiv:1401.1875)
Marais N., 2015, in Corvetti L., Riches K., Schaa V. R. W., eds, 15th International Conference on Accelerator and Large Experimental Physics Control Systems. JACoW, Geneva, Switzerland, p. MOPGF067
Marinakis S., Kalugina Y., Kłos J., Lique F., 2019, A&A, 629, A130
Mattila K., 1986, A&A, 160, 157
Medina S. N. X. et al., 2019, A&A, 627, A175
Meng F. et al., 2019, A&A, 630, A73
Meng F. et al., 2022, A&A, 666, A31
Morello V. et al., 2019, MNRAS, 483, 3673
Morello V., Barr E. D., Stappers B. W., Keane E. F., Lyne A. G., 2020, MNRAS, 497, 4654
Morello V., Rajwade K. M., Stappers B. W., 2022, MNRAS, 510, 1393
Moscadelli L., Sanna A., Goddi C., Krishnan V., Massi F., Bacciotti F., 2019, A&A, 631, A74
Navarro J., de Bruyn A. G., Frail D. A., Kulkarni S. R., Lyne A. G., 1995, ApJ, 455, L55
Neufeld D. A., Wolfire M. G., 2017, ApJ, 845, 163
Ng C. et al., 2015, MNRAS, 450, 2922
Ng C. et al., 2020, ApJ, 903, 81
Offringa A. R., Smirnov O., 2017, MNRAS, 471, 301
Offringa A. R. et al., 2014, MNRAS, 444, 606
Ortiz-León G. N. et al., 2021, A&A, 651, A87
Özel F., Freire P., 2016, ARA&A, 54, 401
Paré D. M., Purcell C. R., Lang C. C., Morris M. R., Green J. A., 2021, ApJ, 923, 82
Parker Q. A. et al., 2006, MNRAS, 373, 79
Partridge B., López-Caniego M., Perley R. A., Stevens J., Butler B. J., Rocha G., Walter B., Zacchei A., 2016, ApJ, 821, 61
Perera B. B. P. et al., 2019, MNRAS, 487, 1025
Perley R. A., Butler B. J., 2013, ApJS, 206, 16
Philippov A., Kramer M., 2022, ARA&A, 60, 495
Pol N., McLaughlin M., Lorimer D. R., 2019, ApJ, 870, 71
Rae K. M., Brown J. C., 2010, in Kothes R., Landecker T. L., Willis A. G., eds, ASP Conf. Ser. Vol. 438, The Dynamic Interstellar Medium: A Celebration of the Canadian Galactic Plane Survey. Astron. Soc. Pac., San Francisco, p. 229
Rajwade K. et al., 2020, SPIE, 11447, 114470J
Ransom S., 2011, Astrophysics Source Code Library, record ascl:1107.017
Ransom S. M., Cordes J. M., Eikenberry S. S., 2003, ApJ, 589, 911

Reid M. J. et al., 2019, ApJ, 885, 131
Reissl S. et al., 2020, A&A, 642, A201
Rigby A. J. et al., 2016, MNRAS, 456, 2885
Risacher C. et al., 2016, A&A, 595, A34
Roy S., Pramesh Rao A., Subrahmanyan R., 2008, A&A, 478, 435
Rudnick L., 2019, preprint (arXiv:1901.09074)
Rugel M. R. et al., 2018, A&A, 618, A159
Ruzmaikin A. A., Sokolov D. D., Shukurov A. M., 1988, Magnetic Fields of Galaxies. Springer-Verlag, Berlin
Rydbeck O. E. H., Elldér J., Irvine W. M., 1973, Nature, 246, 466
Rydbeck O. E. H., Kollberg E., Hjalmarson A., Sume A., Ellder J., Irvine W. M., 1976, ApJS, 31, 333
Sabin L. et al., 2014, MNRAS, 443, 3388
Sandell G., Magnani L., Lada E. A., 1988, ApJ, 329, 920
Saz Parkinson P. M., Xu H., Yu P. L. H., Salvetti D., Marelli M., Falcone A. D., 2016, ApJ, 820, 8
Schilke P. et al., 2014, A&A, 566, A29
Schnitzeler D. H. F. M., Eatough R. P., Ferrière K., Kramer M., Lee K. J., Noutsos A., Shannon R. M., 2016, MNRAS, 459, 3005
Schnitzeler D. H. F. M., Carretti E., Wieringa M. H., Gaensler B. M., Haverkorn M., Poppi S., 2019, MNRAS, 485, 1293
Schuller F. et al., 2009, A&A, 504, 415
Schuller F. et al., 2021, MNRAS, 500, 3064
Serylak M. et al., 2022, A&A, 665, A53
Shanahan R. et al., 2019, ApJ, 887, L7
Shanahan R. et al., 2022, ApJ, 939, 92
Sheffer Y., Rogers M., Federman S. R., Abel N. P., Gredel R., Lambert D. L., Shaw G., 2008, ApJ, 687, 1075
Slabber M. J., Manley J., Mwangama J., Ventura N., 2018, in Guzman J. C., Ibsen J., eds, Proc. SPIE Vol. 10707, Software and Cyberinfrastructure for Astronomy V. SPIE, Bellingham, p. 107070H
Spiewak R. et al., 2022, Publ. Astron. Soc. Aust., 39, e027
Spitler L. G. et al., 2014, ApJ, 790, 101
Spitler L. G. et al., 2016, Nature, 531, 202
Stappers B., Kramer M., 2018, PoS, MeerKAT2016, 009
Stil J. M. et al., 2006, AJ, 132, 1158
Stovall K. et al., 2018, ApJ, 854, L22
Stuardi C. et al., 2020, A&A, 638, A48
Su Y. et al., 2019, ApJS, 240, 9
Szary A., van Leeuwen J., Weltevrede P., Maan Y., 2020, ApJ, 896, 168
Tauris T. M., Langer N., Kramer M., 2011, MNRAS, 416, 2130
Tauris T. M., Langer N., Kramer M., 2012, MNRAS, 425, 1601
Tauris T. M. et al., 2017, ApJ, 846, 170
Taylor A. R. et al., 2003, AJ, 125, 3145
Torne P. et al., 2021, A&A, 650, A95
Truppe S., Hendricks R. J., Hinds E. A., Tarbutt M. R., 2014, ApJ, 780, 71
Umana G. et al., 2021, MNRAS, 506, 2232
Urquhart J. S. et al., 2013, MNRAS, 435, 400
Urquhart J. S. et al., 2018, MNRAS, 473, 1059
Urquhart J. S. et al., 2022, MNRAS, 510, 3389
Vallée J. P., 2022, New Astron., 97, 101896
van der Byl A. et al., 2022, J. Astron. Telesc. Instrum. Syst., 8, 011006
Van Eck C. L. et al., 2021, ApJS, 253, 48
Venkatraman Krishnan V. et al., 2020, Science, 367, 577
Voraganti Padmanabh P., 2021, PhD thesis, Rheinische Friedrich-Wilhelms-Universität Bonn(https://bonndoc.ulb.uni-bonn.de/xmlui/handle/20.500.11811/9336)
Weselak T., 2019, A&A, 625, A55
Wex N., Kopeikin S. M., 1999, ApJ, 514, 388
Wharton R. S., Chatterjee S., Cordes J. M., Deneva J. S., Lazio T. J. W., 2012, ApJ, 753, 108
Whiteoak J. B., Gardner F. F., Hoglund B., 1980, MNRAS, 190, 17P
Xu J., Han J. L., 2019, MNRAS, 486, 4275
Ye H., Gull S. F., Tan S. M., Nikolic B., 2022, MNRAS, 510, 4110
Young E. T. et al., 2012, ApJ, 749, L17
Zhu W. W. et al., 2014, ApJ, 781, 117
Zuckerman B., Turner B. E., 1975, ApJ, 197, 123

APPENDIX A: SENSITIVITY ANALYSIS

In this appendix, we first present analytical sensitivity estimates of the MMGPS in terms of the limiting flux density for finding new pulsars. We then present an analysis of the sensitivity achieved by the pulsar search processing pipeline using the observed and expected S/N estimates for previously known pulsars that were redetected by the survey.

A1 Analytical sensitivity

To estimate the sensitivity of MMGPS-L and MMGPS-S surveys, we use the modified radiometer equation given by (Morello et al. 2020)

$$S_{\rm min} = \frac{{\rm S/N}\,\beta\,(T_{\rm sys})}{G\epsilon\sqrt{n_{\rm pol}\,B\,W_{\rm eff}\,t_{\rm obs}}}\sqrt{\frac{W}{P-W}}, \tag{A1}$$

where G refers to the gain of the telescope and is chosen to be 1.92 K Jy^{-1} that corresponds to the total gain for 40 dishes making up the inner core of the array.[35] The system temperature at L-band ($T_{\rm sys}$) is 27.8 K. This is after taking into account the receiver temperature (18 K) and the sky contribution ($T_{\rm sky}$) of 5.3 K. $T_{\rm sky}$ was derived from scaling the map at 408 MHz made by Haslam et al. (1982) to 1284 and 2406 MHz with a spectral index of −2.6 for L-band and S-band, respectively. The system temperature also accounts for the ground spillover temperature that is 4.5 K at 45° elevation. Similarly at S-band, the system temperature is chosen to be 24 K. This includes the receiver temperature of 22 K and a sky temperature of 2 K following the method applied at L-band. We have not considered the ground spillover at S-band due to lack of experimental data. We have used $n_{\rm pol} = 2$ since two orthogonal polarizations are summed. After accounting for digitization losses for 8-bit data, we have taken $\beta = 1.05$ (Kouwenhoven & Voûte 2001). The integration time $t_{\rm obs}$ is chosen to be 10 min for the MMGPS-L and 20 min for the S-band survey as specified in Table 1 in the main paper. We chose a duty cycle of 10 per cent and applied the scaling relation of $\delta \propto P^{-0.5}$ for spin periods above 10 ms (Kramer et al. 1998). The S/N was chosen as 9 based on the False-alarm probability (see e.g. equation 6.15 from Lorimer & Kramer 2004).

The search efficiency factor ϵ was chosen as 0.7 for fast Fourier transform (FFT) based searching as determined by Morello et al. (2020) for FFT-based searches up to 8 incoherent harmonic sums. We compared the sensitivity estimates between the surveys of MMGPS with legacy Galactic plane surveys like HTRU South low-latitude survey (e.g. Cameron et al. 2020) and PALFA (Cordes et al. 2006) and with the ongoing Galactic Plane Pulsar Snapshot Survey conducted with FAST (Han et al. 2021). Fig. A1 shows a comparison between each of the surveys. The figure shows that MMGPS-S is a factor of 2 more sensitive than the HTRU South low-latitude survey. Similarly, MMGPS-L is about 1.2 times more sensitive than HTRU South low-lat (HTRU parameters are given by Keith et al. 2010). The improved sensitivity over HTRU South low-latitude survey with a lower integration time (637 s versus 4300 s) boosts the probability of several more binary pulsar discoveries. This is because a shorter integration time would be less prone to binary motion effects above the linear acceleration regime. Thus the linear acceleration regime

[35]The inner core alone is used for MMGPS observations to ensure that the filling factor does not drop below a certain level due to narrow beams. Although the inner core consists of 42 antennas, the FBFUSE beamformer kernel requires the number of antennas to be a multiple of 4 for efficient data packing. Hence the observations use 40 dishes.

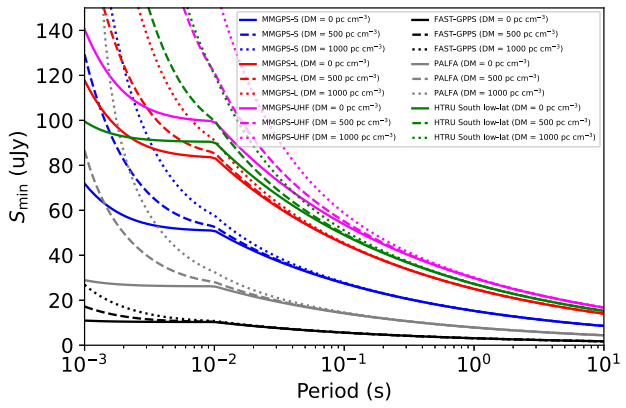

Figure A1. Theoretical flux densities ($S_{\rm min}$) as a function of spin period for current (GPPS, MMGPS-L, MMGPS-S, MMGPS-UHF) and previous (PALFA, HTRU-South low-latitude survey) Galactic plane surveys. The sensitivity curves are calculated at three different DM values (0, 500, and 1000 pc cm^{-3}). The intrachannel dispersive smearing is responsible for different sensitivity limits at different DMs. A minimum detectable S/N of 9 is chosen. The duty cycle is chosen as 10 per cent for spin periods below 10 ms. Above 10 ms, we have used the relation $\delta \propto P^{-0.5}$ (Kramer et al. 1998). The duty cycle conditions used are similar to the analysis made in Han et al. (2021). Effects due to scattering are neglected here.

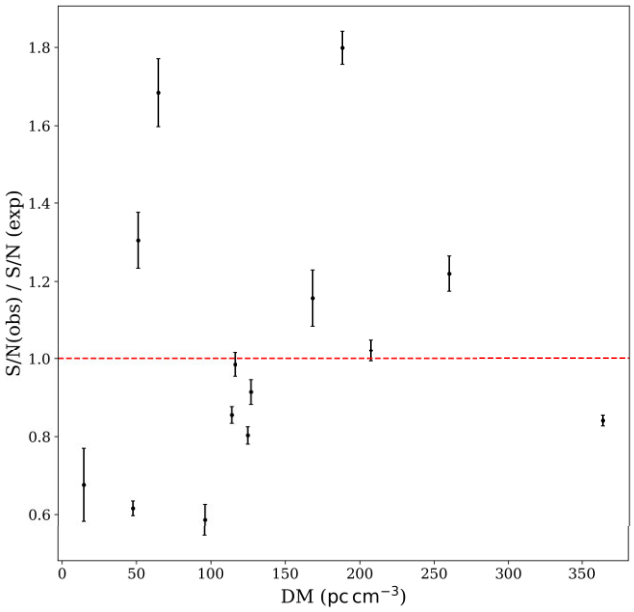

Figure A2. The ratio of the observed S/N and expected S/N plotted against the DM for 14 known pulsars redetected in MMGPS-L and whose flux densities and spectral indices were obtained from Spiewak et al. (2022). The error bars along the *Y*-axis are calculated based on propagation of errors from spectral index and flux density measurements.

is a valid approximation for a wider range of binary pulsar orbits (assuming $T < P_{\rm orb}/10$; see e.g. Ransom et al. 2003). While MMGPS-UHF shows a less sensitive curve than HTRU South low-latitude survey (as seen in Fig. A1), the observing frequency is different. Taking into account the steep spectral index of pulsars, the UHF survey would be at least two times more sensitive than HTRU South low-latitude survey. Furthermore, the reduced integration time (505 s versus 4300 s) makes it effective for discovering several binary pulsars. Although PALFA and GPPS surpass the sensitivity of MMGPS, the survey regions do not overlap. An important point to note is that the numbers are an overestimate of the true sensitivity of the survey. Apart from RFI, red noise arising primarily due to the mains power supply would further reduce the sensitivity especially for long-period pulsars.

A2 Empirical sensitivity

In order to understand if the pulsar search pipeline is performing as expected, we set out to estimate the expected S/N by rearranging equation (A1) for known pulsars that were redetected in the MMGPS-L survey. On comparing the expected S/N with the observed S/N, we get an empirical measure of the sensitivity of the pulsar searches conducted. Although, such an analysis has been conducted by previous surveys in the past (e.g. Barr et al. 2013; Ng et al. 2015; Cameron et al. 2020), conducting such an analysis for MMGPS comes with different caveats.

First, unlike single-dish telescopes like Parkes and Effelsberg, the beam modelling for MeerKAT is different. One needs to account for an offset from the incoherent beam boresight and the offset from the closest synthesized beam to the position of the pulsar. To compensate for this, we regenerated the PSF using MOSAIC (Chen et al. 2021) for relevant observed epochs and reprojected the PSF across the tied array beam tiling for every coherent beam position. We then estimated a weighted offset factor W as

$$W = f_1 f_2, \tag{A2}$$

where f_1 is the fractional gain obtained from a Gaussian offset factor based on how far the pulsar position is from the boresight of the incoherent beam, and f_2 is the fractional gain based on the offset between the pulsar position and the synthesized beam tiling pattern weighted by the generated PSF. This weighted offset factor was multiplied to the expected S/N value.

Secondly, the high bandwidth (856 MHz) used for the MMGPS-L implies that the contribution of the spectral index of the pulsar becomes significant in determining the weighted flux density across the frequency band. To resolve this issue, we obtained spectral index and flux density measurements from pulsars reported by Spiewak et al. (2022) who used the same instrument (MeerKAT) and receiver (L-band) to obtain these measurements. We then cross-matched the set of MMGPS-L known pulsar redetections with the set of pulsars reported by Spiewak et al. (2022) leaving 14 common known pulsars. To make the analysis further robust, frequency masks applied for each of the considered redetections were also accounted when estimating the effective bandwidth. Fig. A2 shows the ratio of observed to expected S/N for the 14 pulsars as a function of their DM values. As evident from the plot, pulsars with DM below 100 pc cm^{-3} show much more variability about the ideal ratio of unity. This can be attributed to scintillation across time and frequency leading to larger variability in fluxes and in turn the observed S/N. One of the outliers above DM of 100 pc cm^{-3} is a pulsar whose position lies in between beams possibly leading to an unmodelled surge in the PSF beyond the half-power boundary. This is not surprising given that the PSF is known to show more variability in fractional sensitivity and is not well modelled. Except for these few outliers, the overall distribution hinges close to the ideal sensitivity line within a 20 per cent margin. There are multiple other factors that can tamper with the expected sensitivity of pulsars and have not been incorporated in the analysis effectively. First, the beamforming efficiency is assumed to

be 100 per cent. Estimating the true efficiency is a tedious task given that comparing the coherent beam power with incoherent beam power needs to account for fine intricacies in the beamforming process including true antenna weights and an unstable gain across frequency. Secondly, apart from standard frequency masks, each file undergoes RFI excision based on multiple filters applied from the PULSARX tool. There is no clear handle of the fraction of data that are filtered based on this tool and this value changes from observation to observation.

Keeping these points in mind and given that the survey has already made 78 new discoveries, we can safely say that the survey does not have any outstanding sensitivity issues. In the future, we aim to expand the number of known pulsars in this analysis to a larger number in order to obtain a more robust plot. This analysis will be published elsewhere.

This paper has been typeset from a TEX/LATEX file prepared by the author.